

Developing the orthotropic linear-elastic model for wood applications using the FE method

Tarik Chakkour and Patrick Perré

Université Paris-Saclay, CentraleSupélec, Laboratoire de Génie des Procédés et Matériaux, Centre Européen de Biotechnologie et de Bioéconomie (CEBB), 3 Rue des Rouges-Terres, 51110 Pomacle, France
E-mail: tarik.chakkour@centralesupelec.fr

August 23, 2024

Abstract. The purpose of this work is to develop the three-dimensional (3D) finite element (FE) modeling approach for the linear mechanical behavior of the wood material. The developed framework consists of implementing the 3D constitutive equations using the linear elasticity theory. Wood is a complex, porous, fibrous, inhomogeneous, highly anisotropic material. Various wood materials are considered, such as poplar, spruce, and maple specimens to validate the applicability of the FE modeling. The framework is implemented in an explicit code, written in Fortran language, and based on the PETSc library. To that purpose, the up-scaling methods, such as the homogenization technique that allows the prediction of the macroscopic property of materials, in our case the effective Young's modulus, is investigated. A numerical approach to control the equivalent micromechanical properties is presented using a representative elementary volume (REV) concept. Here, we investigate the convergence trend of material properties and structural geometries according to REV size. This framework aids considerably in predicting the mechanical properties of a given material microstructure. In order to determine the mechanical properties of the wood material in its anisotropic direction, the traction and compression loadings were performed using numerical tests. The FE modeling of some cases is presented for the final validation.

Keywords: Elasticity, orthotropic, finite element method, wood, CT scan 3D morphology.

1 Introduction

Wood is a natural composite material with rich and excellent mechanical properties such as its low density [1, 2]. Some wood is hard, containing fibrous tissue due to physical hardness or density. These fibers are robust in tension and emmersed in matrix lignin to be resist for compression. Wood is also a heterogeneous, anisotropic, and variable material with a complex structure which covers various length scales. This anisotropic property [3, 4] explains the dependency of the mechanical properties on its material directions [Radial (R), Tangential (T), Longitudinal (L)] and differs among species. This heterogeneity means the huge stiffness changeability encountered in wood. In order to express this complex feature, multiscale frameworks have been developed on finite element simulations with computational homogenization aspect. It is used for generation in numerous applications [5, 6, 7], such as building, construction, transportation, and landscaping timbers. In order to completely utilize the potentiality of the wood material, ameliorate knowledge of its mechanical behavior and constitutive frameworks are essential.

Over the last few years, wood has emerged as a promising material due to its significant and practical applications [8, 9]. It has captivated many researchers for its superior mechanical properties. They have provided much effort to investigate its large variability from these macroscopic material properties. The objective is to avert the requirement for essential safety factors derived from the high unprofitable cost of timber members in these applications. Providing a comprehensive about microstructural properties of individual wood specimens is required to correspond to them at the macroscale. The properties of these equivalent homogeneous materials are determined by employing homogenization techniques [10, 11]. The link between these scales prepares accurate and compatible sets of macroscopic characteristics of wood in orthotropic direction.

There are two main sorts of wood cell, earlywood and latewood, also specified as tracheids, and they are devoted considerably to the volume of softwoods [12, 13]. When the favourable climatic conditions meet, there is a high growth rate of the earlywood cells that laid down in the spring season [14, 15]. However, the latewood cells are formed in the late summer, when the rate of growth decreases [16, 17]. They provide mechanical strength with different characteristics. The cell walls subject to the earlywood are thin with a large open pore space, while those of the latewood are thick with smaller pore space. Büyüksarı et al. [18] investigate the determination of the mechanical properties from the earlywood and latewood sections in standard size samples with comparing the computed and measured mechanical properties.

Our primary motivation for developing the framework is to exploit the 3D imaging techniques, including X-ray computer tomography (CT) and magnetic resonance imaging (MRI). These techniques offer many conveniences, resulting from significant improvements in high-resolution and reconstruction strategies. One technology that has benefited from such improvements is X-ray tomography. This technology is based on using different radiographs from a given object, viewed at various angles, to construct a bidimensional slice of that object. This paper will consider the conventional μ CT imaging [19, 20, 21] to highlight many aspects of wood anatomy, in particular, a comprehensive characterization of the wood

formation and its reconstruction of the geometric structure.

When determining the homogenization approach established on Finite Elements Method (FEM), the mechanical behavior of wood materials is usually expressed by using Representative Elementary Volume (REV) [22, 23]. This modeling is aimed at analyzing the behavior of heterogeneous wood structures as it allows making the problem simple by examining a sub-volume of a total structure, without influencing the precision of the results [24, 25]. Particularly, the homogenized field variables of a material wood on the macroscopic scale depend on its size, yielding the effect of REV size questionable. The definition of REV has endured hard in the literature for properties related to linear elastic models. The homogenization approach will notice the consequence obtained here since the micromechanical response at each sample point relies on the macroscopic deformation. In the beginning, the concept of REV analyses was presented by Hill (1963). According to a continuum mechanics viewpoint, the REV must contain an adequately large number of heterogeneities. Therefore, this work aims to investigate the convergence of the macroscopic elastic properties [26, 27] by ensuring an appropriate choice of the REV size. This volume REV is subjected to specific meshing criteria to satisfy the convergence behavior. Some researchers have investigated various types of REV, for example, Gonzalez and Llorca [28], studied a square REV, which composes a homogeneous and random dispersion of fibers included in the polymeric matrix. The work [29] is devoted to determining the adequate characteristics of a REV to perfectly model the mechanical behavior of a unidirectional glass fiber-reinforced polymer composite.

The present contribution is aimed at providing a simplified tool to determine the properties of the deformed microstructure with high computational efficiency based on the PETSc library [30], widely used in various other packages [31, 32]. This library is considered popular and suitable for determining solutions of partial differential equations (PDE). It provides conveniently vast flexibility for users, that includes parallel linear and nonlinear solvers [33, 34]. Many previous works [35, 36, 37] on deformation microstructure have been carried out in which the microstructure is influenced by phase compositions and processing parameters. In the present improvement, the global matrix associated with this discretization is stored in the sparse format supported by PETSc. This implementation focuses on the compressed sparse row (CSR) storage [38, 39, 40, 41] which defies scientific computing due to its efficiency allowing robust storage. The computational cost for this storage grows linearly depending on the system size, with some benefits. These benefits consist of reducing the memory overhead and avoiding storing zero elements. This benchmark problem illustrates the accuracy [42, 43, 44] of the proposed strategy to linear elasticity.

The rest of the paper is structured as follows. Section 2 presents a simple way to obtain wood morphology from tomographic images. Then, the image-analysis techniques are used to give the morphology distributions and extract morphological details. This Section describes briefly the implemented FEM framework for orthotropic elastic problems. Section 3 reports the numerical results of testing a wood structure with highlighting 3D mechanical analysis. The homogenization approach for equivalent elastic behavior of wood species is used to perform the model framework but further a multi-scale simulation tool. Finally, Section 4 concludes this work.

2 Materials and methods

This section is devoted to describing the main workflow for how to provide the binary representation of the wood morphology. The choice of studying these wood sample species is motivated by porosity, anisotropy, and heterogeneity material characterized by some structural anomalies. All the specimens' preparation and conditioning will be detailed. For modeling the structures in anisotropic materials, the tool most often used is the general purpose FE tool. This section aims to describe mathematically this tool which is specifically designed for anisotropic materials to simulate small deformations.

2.1 Tomography and segmentation

The scanning lab tomography is used to obtain a stack of images to capture the structure of each morphology. X-ray nano-tomography is exploited as a one tool available to wood anatomists to study the three-dimensional organization with a high-resolution image result. In order to carry out the segmentation of the 3D representation from these stack images by the reconstruction software, further processing is required using various software. The image processing is conducted by general software such as Avizo, Matlab, Python, etc. Fiji [45] is one of the practical software used in the current work to identify objects and study their properties based on the acquired images. Fiji is an extension of the ImageJ [46] and ICY [47] softwares. It is a software package that offers a wide range of plugins for enhancing image visibility. The purpose of this study is to provide quick image treatment by selecting the Thresholding tool. The automatic thresholding method of Otsu [48] proposed by Fiji is one possible approach to get the binary image. The Fiji process menu offers a wide range of easy-to-use binary tools, such as a filter to remove noise or control a threshold value [49, 50]. The aim is to identify and separate the present two phases (gas and solid) and generate the morphology's tetrahedral mesh [51].

The wood samples are acquired by X-ray nano-tomograph EasyTomXL Ultra 150-160, RX Solutions. 2D-projection images are realized by measuring the X-ray attenuation originated from a selection. The system is equipped with a nano-focus source with different detector types for both fast and in-situ (flat panel detector) and high-resolution scanning (CCD camera). The scanning resolution is the order of $1 \mu m$ and takes at least four hours. Fig. 1 depicts the full scan of the wood samples, which are with a diameter of about 1 mm, the radius and height of this cylinder are represented by 2.82 and 3.11 millimeters, respectively. The image file sizes are extremely large, which forces an adequate ROI (Region of Interest) to be chosen within the sample. This sub-volume is a parallelepiped whose center and dimensions should be selected. Each parallelepiped sample is treated with ImageJ-Python software to make 3D volumic reconstruction possible. The post-processing of 3D reconstructed wood specimens is presented in Fig. 2, which is shared into six diagrams. The top three diagrams 2a-2c show that each sample is a randomized phase two study. The first is associated with the gaseous phase, and the second is for the solid phase (matrix). Since the free water occupied by the gaseous phase does not interact with the solid one, the porosities do not lead to mechanical variations. Then, the displacement field basis of all the solid matrix nodes is

considered to neglect the gas distribution in the pore space. However, diagrams 2d-2f depict the extracted solid phase from the same 3D reconstructed wood specimens. For this reason, only the mesh of solid phase has been implemented in the finite element software.

2.2 Elastic properties for model material

We assume that the mechanical properties used in the model are considered constant and independent of the porosity. This hypothesis is justified in simplifying the modeling work. The aim is to find the better parameters existing in the literature for which the model is convergent and affects the numerical results. The ultrastructural parameters reported for wood materials are a collection of different values of engineering elastic constants. These values are computed from molecular models [52, 53] or predicted from the behavior of similar materials [54, 55]. Neagu and Gamstedt [56] focus mainly on the knowledge of the wood fiber structure by providing these hygroelastic properties from some wood samples. These properties are important information used essentially in the FE calculations [57]. The mechanical parameters to identify the solid phase for these species, poplar, spruce, and maple samples, are described as follows. Note that the hygroelastic properties of the cell wall layers are computed with the recursive algorithm of Sutcu [58] must be given as input to the mechanical model presented in terms of physical units Gigapascal (GPa). The longitudinal Young's moduli E_L of wood specimens is equal to 64.0 GPa, while the cell wall and lumen are obtained from the radial and tangential Young's modulus E_R and E_T using the same value 6.08 GPa, i.e., $E_L = 64.0$ GPa, $E_R = E_T = 6.08$ GPa. Due to the transversely isotropic elastic properties, the Poisson's ratios ν_{TL} and ν_{RL} , the shear moduli G_{TL} and G_{RL} , are the same, i.e., $\nu_{TL} = \nu_{RL} = 0.03$, $G_{TL} = G_{RL} = 2.54$. The Poisson's ratio ν_{RT} and the shear moduli G_{RT} , for transverse strain in the tangential direction (T) when stress applies in the radial direction (R), are 0.42 GPa and 2.14 GPa, respectively, formally, $\nu_{RT} = 0.42$ GPa, $G_{RT} = 2.14$ GPa.

2.3 Up-scaling procedure

One of the important challenges in the FEM framework is enforcing the boundary conditions. The penalty method has been proposed [59, 60] to control this problem. This method offers an approximation for boundary conditions. The benefit of this method is that there are no further global constraint equations and only one unknown, which is the displacement field [61, 62]. Note that the penalty parameter involved in the implementation has to be larger, exceeding the other elements of the stiffness matrix [63]. Hadjicharalambous et al. [64] showed the high accuracy and good convergence from the present penalty method with some concrete numerical examples. They tested this convergence by increasing the degrees of freedom and analyzing the global system matrix. This choice leads to good convergence according to a refined mesh. Considering a 3D material microstructure in form of cubic shape, subjected to uniform displacement on its one particular face following the orthotropic direction as shown in each diagram of Fig. 3. In the following, the penalty method is applied and validated under three computational homogenization scenarios in wood materials. Each

scenario means that a loading is applied with taking into account the boundary conditions for uniaxial loading cases. When the displacement is applied at one face, for instance the upper face normal to the longitudinal direction (L), as shown in the left diagram, all the lateral and lower faces stay blocked to capture much-averaged values. This means that the penalty method is operated to apply a null displacement at these faces, and also the targeted displacement. To validate the purpose of the homogenization approach, this strategy is continued with imposing the associate displacements in the transverse plane (R,T), as illustrated in the middle and right diagrams.

Let Ω be the domain of a body and $\partial\Omega$ its boundary disjointly defined by the surfaces Ω^u and Ω^t , which are related to Dirichlet's and Neumann's boundary conditions. It means that the boundary $\partial\Omega$ is subdivided into two parts Ω^u and Ω^t , i.e., $\partial\Omega = \Omega^u \cup \Omega^t$, $\Omega^u \cap \Omega^t = \emptyset$. The mixed fundamental boundary value problem of linear elastic model aims to determine the distribution of stress σ , strain ϵ and displacement \mathbf{u} throughout the body, when it has constrained displacements $\bar{\mathbf{u}}$ defined on Ω^u and is loaded by an external system of distributed surface and body forces with densities denoted by \mathbf{t} on Ω^t and \mathbf{f} in Ω , respectively. In what follows, we will introduce the governing equations for solving the problem of linear elasticity. These equations are used to solve the elasticity problem on the REV model including the balance equation interfaced with boundary conditions for non-homogeneous material. The REV occupies the computational domain. Denoting Ω the REV domain and V is the volume of the REV. In the model, displacements and the tensions are supposed to be continuous across interfaces, meaning that all the phases presented in REV model is superbly bonded. Thus, the constitutive equations modeling the linear elastic problem can be formulated as,

$$\begin{cases} -\text{div}(\sigma) = \mathbf{f} & \text{in } \Omega, \\ \mathbf{u} = \bar{\mathbf{u}} & \text{on } \Omega^u, \\ \sigma \cdot \mathbf{n} = \mathbf{t} & \text{on } \Omega^t. \end{cases} \quad (1)$$

In which σ is the stress tensor and \mathbf{f} is the body force vector. The vector \mathbf{t} represents the tension load on part of the static boundary Ω^t prescribed by the value $\|\mathbf{t}\|$ and \mathbf{n} is the exterior unit normal on the boundary Ω^t . It is well established that the mechanical properties of wood materials depend on their orientation. Mechanics of wood materials usually describe longitudinal and transverse directions related to its structure, which are described in Fig. 3. The orthotropic wood models consider different material behavior for each orthogonally related direction. Consequently, more parameters are requested to report material behavior fully compared to isotropic materials. Unlike isotropic materials that are parameterized by a unique Young's modulus and Poisson's ratio, orthotropic materials have three various Young's moduli E_1, E_2, E_3 , one for each orthogonal direction, and six Poisson's ratios ν_{ij} , for $i \neq j$, only three of which are independent. In order to keep the elasticity tensor matrix \mathbf{C} symmetric, the Poisson's ratios have to satisfy

$$\frac{\nu_{ij}}{E_i} = \frac{\nu_{ji}}{E_j}, \quad i, j = 1, 2, 3. \quad (2)$$

Assuming that the physical variables belong to the microscale problem, that is, are related

to the geometry and material of the volume REV. Denoting \mathbf{C} and \mathbf{B} by the matrices of elasticity and partial derivatives of the interpolation functions. The strain ε and stress σ tensors could be expressed in term of the displacement \mathbf{u} as,

$$\varepsilon = \mathbf{B}\mathbf{u}. \quad (3)$$

$$\sigma = \mathbf{C}\mathbf{B}\mathbf{u}. \quad (4)$$

The stiffness matrix \mathbf{C} , the fourth-order tensor of orthotropic wood materials show elastic constants, which can be presented in the following form: $\sigma = \mathbf{C}\varepsilon$,

$$\begin{bmatrix} \sigma_{11} \\ \sigma_{22} \\ \sigma_{33} \\ \sigma_{12} \\ \sigma_{23} \\ \sigma_{13} \end{bmatrix} = \begin{pmatrix} \frac{1-\nu_{32}\nu_{23}}{E_2 E_3 \Delta_c} & \frac{\nu_{12}+\nu_{13}\nu_{32}}{E_2 E_3 \Delta_c} & \frac{\nu_{13}+\nu_{12}\nu_{23}}{E_2 E_3 \Delta_c} & 0 & 0 & 0 \\ \frac{\nu_{12}+\nu_{13}\nu_{32}}{E_1 E_3 \Delta_c} & \frac{1-\nu_{13}\nu_{31}}{E_1 E_3 \Delta_c} & \frac{\nu_{23}+\nu_{21}\nu_{13}}{E_1 E_3 \Delta_c} & 0 & 0 & 0 \\ \frac{\nu_{13}+\nu_{12}\nu_{23}}{E_1 E_2 \Delta_c} & \frac{\nu_{23}+\nu_{21}\nu_{13}}{E_1 E_2 \Delta_c} & \frac{1-\nu_{21}\nu_{12}}{E_1 E_2 \Delta_c} & 0 & 0 & 0 \\ 0 & 0 & 0 & 2G_{12} & 0 & 0 \\ 0 & 0 & 0 & 0 & 2G_{23} & 0 \\ 0 & 0 & 0 & 0 & 0 & 2G_{13} \end{pmatrix} \begin{bmatrix} \varepsilon_{11} \\ \varepsilon_{22} \\ \varepsilon_{33} \\ \varepsilon_{12} \\ \varepsilon_{23} \\ \varepsilon_{13} \end{bmatrix} \quad (5)$$

where the term Δ_c is defined as,

$$\Delta_c = \frac{1 - \nu_{21}\nu_{12} - \nu_{31}\nu_{13} - \nu_{32}\nu_{23} - \nu_{12}\nu_{23}\nu_{31} - \nu_{21}\nu_{13}\nu_{32}}{E_1 E_2 E_3}. \quad (6)$$

\mathbf{C} is the Hooke's matrix associated with the stiffness form of linear elastic Hooke's law. The stiffness operator is represented by a 6×6 symmetric matrix whose elements are expressed in equality (5). In our case of a fully anisotropic elastic material, 9 independent terms are required to fill the matrix \mathbf{C} . Denoting V_Ω^0 is the set of continuous and sufficiently regular functions, zero-valued in Ω^u . Multiplying the first expression of Eq. (1) by a test function \mathbf{v} lying in the space V_Ω^0 of kinematically admissible displacements at zero, and next integrating by parts. In this context, the resolution of the elasticity problem consists of determining the displacement field \mathbf{u} corresponding to the solution of the following variational problem,

$$\int_\Omega \mathbf{C}\mathbf{B}\mathbf{u} : \mathbf{B}\mathbf{v} \, d\Omega = \int_\Omega f\mathbf{v} \, d\Omega + \int_{\Omega^t} \mathbf{t} \cdot \mathbf{v} \, ds. \quad (7)$$

Based on the established micromechanical modeling, the homogeneous finite element simulation of REV models is carried out. The REV models of the rised voxels size with different volume fractions are established, and its effective stiffness are calculated by using numerical homogenization calculation technique. By combining the numerical homogenization computation technique, the effective stiffness property was predicted. To investigate the mechanical effects from the homogenized behavior, the uniaxial tests are considered. It consists of doing uniaxial tensile tests. Fig. 3 depicts the schematic diagram of building the loading method adopted in the tensile test process. A constant displacement is applied to the sides of the specimen following the direction loading. The macroscopic stress and strain tensors $\bar{\sigma}$ and $\bar{\varepsilon}$ of the macroscopic homogeneous REV model can be computed by averaging the microscopic

variables or local stress and strain σ and ε over the entire volume of REV, and expressed according to micro-macro relation,

$$\bar{\sigma} = \frac{1}{V} \int_{\Omega_s} \sigma \, dV. \quad (8)$$

$$\bar{\varepsilon} = \frac{1}{V} \int_{\Omega_s} \varepsilon \, dV. \quad (9)$$

In which Ω_s is the solid phase of all the microstructure REV. The homogenized strain $\bar{\varepsilon}_{\text{Th}}$ is computed exactly from the imposed displacement field. This choice is motivated by taking into consideration the repartition of pores, particularly their volumes. The macroscopic properties of a wood material, are partially controlled by the material property contrast between the solid and porosity phases. The macroscopic strain yields a homogeneous deformation on the REV, which is imposed by a displacement. The result $\bar{\varepsilon}_{\text{Th}}$ is presented for the average support displacement $u_{\text{Dirichlet}}$ over the support length L_s , defined as,

$$\bar{\varepsilon}_{\text{Th}} = \frac{u_{\text{Dirichlet}}}{L_s}. \quad (10)$$

Let $\bar{\mathbf{C}}$ be the homogenized effective stiffness tensor. In reality, $\bar{\mathbf{C}}$ should be considered as a 6×6 matrix. Since three computed homogenized material constants of the shear moduli are not involved in our computational homogenization procedure, the effective elasticity matrix $\bar{\mathbf{C}}$ will be of 3×3 elements. The numerical modeling effort is performed using three series of computational homogenization analyses. Then, the homogenization method for heterogeneous media is carried out meaningfully to estimate the three effective elastic properties. The effective stress-strain relation for the averaged stress and strain can be written as,

$$\bar{\sigma} = \bar{\mathbf{C}} \bar{\varepsilon}_{\text{Th}}. \quad (11)$$

Denoting by $\bar{\sigma}_{ij}$ the volume average of the corresponding stress component in REV. Under the radial loading, the first line of the averaged stiffness matrix $\bar{\mathbf{C}}$ can be calculated as,

$$C_{11} = \frac{\bar{\sigma}_{11}}{\bar{\varepsilon}_{\text{Th}}}, C_{12} = \frac{\bar{\sigma}_{22}}{\bar{\varepsilon}_{\text{Th}}}, C_{13} = \frac{\bar{\sigma}_{33}}{\bar{\varepsilon}_{\text{Th}}}. \quad (12)$$

Similarly, from the tangential and longitudinal loadings, we can completely fill the matrix $\bar{\mathbf{C}}$,

$$\bar{\mathbf{C}} = \begin{pmatrix} C_{11} & C_{12} & C_{13} \\ C_{21} & C_{22} & C_{23} \\ C_{31} & C_{32} & C_{33} \end{pmatrix}. \quad (13)$$

By inverting the constitutive matrix defined by (13), the compliance matrix $\bar{\mathbf{S}}$ is gotten. Then the effective elastic constants of REV can be calculated according to the matrix $\bar{\mathbf{S}}$. Particularly, the effective Young's modulus E_1^h , E_2^h , and E_3^h are exactly the inverse of diagonal elements of $\bar{\mathbf{S}}$,

$$E_1^h = \frac{1}{C_{11}}, E_2^h = \frac{1}{C_{22}}, E_3^h = \frac{1}{C_{33}}. \quad (14)$$

The strictly lower triangular part from matrix $\bar{\mathbf{C}}$ is used to obtain the three effective Poisson's ratios ν_{12}^h , ν_{13}^h , and ν_{32}^h . However, the normalized effective Young's modulus ν_{21}^h , ν_{31}^h , and ν_{23}^h are deduced from the strictly upper triangular part. Due to the symmetry of matrix $\bar{\mathbf{C}}$, these ratios satisfy the proportionality equation defined by (2). Formally,

$$\nu_{12}^h = -C_{21}E_1, \nu_{31}^h = -C_{13}E_1, \nu_{32}^h = -C_{32}E_3. \quad (15)$$

The up-scaling procedure aims to train material wood models for the homogenization responses. The microscale REVs are then subjected to three various loadings, and the responses are recorded and used to validate the macroscopic data-driven model. For completeness, we give a summary of this procedure and the applications to computational anisotropic mechanics problems. Our computational process often involves the following steps:

- First, the computational domain is decomposed into small tetrahedral elements of four points, and each point has three degrees of freedom.
- Then, the local stiffness matrix for each element is of size 12×12 . Each local matrix is presented by three unidimensional vectors satisfying the optimization procedure to avoid storing the nonzero entries of the matrix. The local element stiffness matrix can be determined in terms of the discrete matrix \mathbf{B} and \mathbf{C} given in equalities (3)-(5).
- The assembly process consists of taking into account all the elementary contributions. Each local system determines each contribution to build a global linear system.
- The applied displacement on the boundary is considered by updating the coefficient of the global matrix, which is presented in a sparse format. These boundary conditions are incorporated in the FE formulation via the invoked penalty method. Finally, the global linear system is solved with PETSc in parallel using a KSP (Krylov subspace accelerators) solver to determine the unknown displacement field.
- The application of homogenization for stress-strain behavior is demonstrated. The macroscopic elastic properties are determined via micro-to-macro scale transition analysis. Particularly, the macroscopic stress $\bar{\sigma}$ and strain $\bar{\varepsilon}$ tensors are estimated in a discrete assembly via relations (8)-(9).

The stages mentioned in Fig. 4 summarize the resulting computational homogenization leading to the upscaling of microscopic scale towards a macroscopic for one specific loading [65, 66]. During the loading process restricted to three anisotropic directions, three homogenization schemes are grouped and factorized [67, 68] via equality (11). The explicit expressions of the effective elastic properties are computed using equalities (14)-(15) based on the matrix $\bar{\mathbf{C}}$.

3 Results and discussion

This section aims to demonstrate the capability of a finite deformation approach for analyzing elastic orthotropic materials. For modeling the structures in anisotropic materials, the tool most often used is the general purpose FE tool described in subsection 2.3. This standard approach can be used for different categories of materials and their properties. This model is validated for the wood specimens. The realistic loading is applied at the microstructure volume during the deformation process. The deformed REV is exhibited and analyzed in terms of the realistic microstructure. As a simple rule based on the presented curve shape, we used the range of deformation [0%, 3%] for all mechanical tests.

3.1 Numerical test

This part is devoted to illustrate the ability of the finite element method (FEM) framework to be functioning. First, this framework predicts the mechanical properties, particularly the nodal displacements in the standard orthotropic directions for the poplar, maple, and spruce wood specimens. This framework is validated against some uniaxial mechanical testing systems responding to the tensile loadings. Fig. 5 depicts the displacement field at each test following the orthotropic direction. The material is assumed to be elastic and homogeneous, and is determined by mechanical properties, including elastic properties described in Subsection 2.2. The Dirichlet boundary conditions have been defined by applying an horizontal displacement on the top lateral face following the radial direction (R), and by blocking the bottom lateral face, as shown in diagram 5a. There is a null displacement on four rest faces. The strain ε_{11} in the R-direction is computed according to the strain-displacement relation (3). From this, and according to the stress-strain equality, the component of stress σ_{11} is computed. Next, the stiffness matrix S is utilized to evaluate the transverse strains. Then, the elementary displacement field \mathbf{u} is determined in terms of strain ε , using an integral operator given by equality (3). The component of resulted displacement \mathbf{u}_{11} is illustrated in diagram 5a. Similarly, the same situation occurs for the tangential \mathbf{u}_{22} and longitudinal \mathbf{u}_{33} displacements as shown respectively in diagrams 5b-5c. The displacements \mathbf{u}_{11} , \mathbf{u}_{22} , and \mathbf{u}_{33} in their orthotropic directions grow linearly with each direction. The model demonstrates that it is consistent with respect to the expected calculation proving the Poisson effect consequently. Each displacement varies progressively from the lower value, which is presented by the bottom color of the scale to the higher value given by its top where the force is applied.

From a morphological point of view, the deformation intrinsically characterizes the new state of the object. It is necessary to compare the transformation and shape between the original object and the deformed one. For instance, in such fields as neurosurgery [69, 70], the deformed object permits predicting a tumor’s growth. Further, the behavior of forward deformation models is investigated in [71, 72] to predict the variations in human tissue characteristics in response to the movement of bones. The current results are reported and used to verify the proposed method by interpreting the deformed. The main objective is to analyze deeply the deformed paths with the simulation tests in three-dimensional viewing. Only one typical test of these simulations is performed using the uniaxial tensile test. Several

influencing factors should be considered when testing configurations are realized within the framework model. These tests contribute to evaluating the accuracy of the deformed field from the original microstructure.

Fig. 6 depicts the microscopic deformation subjected to the orthotropic tensile loadings. Each mechanical test presents a response under uniaxial loading. The loadings follow the radial (**R**), tangential (**T**), and longitudinal (**L**) directions, corresponding respectively to the poplar (see diagram 6a), maple (see diagram 6b), and spruce (see diagram 6c) wood specimens. The deformation provides information about the new structure and its visualization is an important step. The analyzed deformed demonstrates that no enlargement occurs in the transversal plane. The profile in the deformed state differs a little from the original microstructure presented in the initial state since the lateral faces are blocked. The enlargement is remarked during each test following the uniaxial orthotropic direction normal to this the transversal plane. The 3D observations bring a qualitative overview of the poplar and maple microstructures, little raising the shape and size of the porosity. The poplar's and maple's pores elongate in the principal direction without contracting perpendicularly. However, for the spruce specimen loaded in the longitudinal direction, the distribution of pores becomes uniform. This deformed structure has provided the natural response of this expected elastic behavior. The deformation of the specimen becomes considerable, and its damage happens early when an important displacement field is imposed.

3.2 Convergence test

Choosing a Representative Elementary Volume (REV) is a crucial step in modeling to correctly describe the material's microstructure. There is not a unique and request concept of the REV for a heterogeneous material with complex microstructures. That might describes the existence of different definitions of the REV, see [73] for a review. Many approaches have been investigated in the literature to decide this size. According to Hill [74], the REV must contain sufficient heterogeneity and its size must be much larger than the characteristic length of the microscale and small enough concerning the macroscopic scale of the material. A statistical framework based on the convergence of the effective properties is investigated in [75, 76] to determine the size of the volume REV. In this contribution, our approach is made by evaluating the visible characteristics of the material by executing various numerical computations on different sizes of the microstructure.

The evaluation of the REV size in computational homogenization is approached by treating mechanical response quantities in terms of mesh type to utilize their properties. A novel approach to determining the convergence of effective properties as a function of domain size is explained as follows. This approach is often recommended in material science, since it converges faster with increasing the number of tetrahedral cells. Its accuracy is demonstrated through three main meshing tests, which are carried out for each wood specimen with a fixed REV size. To achieve higher accuracy and convergence rates of the standard FE method, especially in the presence of complex meshes [77, 78, 79]. Three types of mesh are investigated. In this contribution, we study the convergence and stability from the mesh research until the mechanical effective quantities become stable. The flow chart of the proposed procedure

is shown in Fig. 7. Given a wood sample, we employ multiple mesh types via a progressive refinement strategy, avoiding morphology and topology modification. From a more practical standpoint, the idea touched upon here is considered in the smoothing stabilization and the FE discretization. According to the wood specimen and its REV size, the adaptive mesh is regulated following the refinement process to capture reasonable convergent macroscopic values. Once the suitable computed mesh has converged, the proportionality rule from a given sample resolution is made to determine the convergent mesh without running any simulation.

The numerical tests are selected by augmenting the grid resolution, presented in Fig. 8 to show the convergence of the numerical method. The pores are maintained to be sufficiently smoothly meshed. The first is obtained with the coarse mesh; the second is realized with the medium mesh; and finally, the last is acquired with the refined mesh. A set of informations concerning the three meshes given in Tab. 1, for the spruce and poplar specimens. The microstructure of the intermediate spruce species is displayed below. This states that the initial mesh is around 228791 volumic cells, and the final mesh reaches around 540729. It also displays the effective elastic modulus in the radial and tangential directions. Since the poplar and maple have the same characteristics of vessels, the procedure testing is repeated sufficiently for the poplar wood with REV size, which is $385 \times 385 \times 6$ voxels.

In summary, the above study introduced an adaptive meshing framework that was based on a refinement technique to guarantee convergence to corresponding values. The convergence criteria of the two specimens were estimated following the steps of the invoked strategy. First, these specimens were homogenized in terms of a three-dimensional mesh of the REV size. Three levels of refinements are investigated to converge to the final solution. During the refinement process, the mesh varies by conserving the same morphology and the volume fraction of the aggregates. Then, in the second step, the effective mechanical values were compared. The variation of aggregate meshing from coarse to medium impact insignificantly until stabilizing at the converged values. As a result, it can be seen that the coarse mesh is sufficient in terms of the existing domain size used in the calculations. The key idea is to inspire from this study to the next one to choose according to the REV size, the convergent mesh. The next study follows further development, particularly complex block calculation with largest REV, which is much more time-consuming.

In this part, a convergence test was handled to determine the REV sizes whose values satisfy the stability of the effective mechanical property. The computation is carried out in the case of the standard wood directions. The studied REV sizes are considered within the full 3D image of each sample. P. Perré et al. [80] have used a similar approach to conduct a convergence test regarding numerical experiments concerning thermal conductivity. In our case of spruce, we will demonstrate that the established REV does not impact the convergence behavior. Consider the user input center (x_0, y_0, z_0) to select the REV geometry. This REV is investigated in parallelepiped form with dimensions $(2\Delta x, 2\Delta y, 2\Delta z)$, given as follows:

$$\begin{aligned} \text{REV}_i &= [x_0 - \Delta x, x_0 + \Delta x] \times [y_0 - \Delta y, y_0 + \Delta y] \times [z_0 - i \times \Delta z, z_0 + i \times \Delta z], \\ i &= 1, \dots, 20. \end{aligned} \tag{16}$$

At each test, the volume of the REV is simultaneously increased in the longitudinal direction following the same step $\Delta z = 5$, but fixed in the transverse plane (R,T), i.e., $\Delta x = \Delta y = 96$. The information concerning the mesh, such as the computed solid fractions and the volumic cell numbers, are presented in Tab. 2. The predicted macroscopic Young's modulus are given in the same table. The convergence is noticed in the middle volumes as the REV size is a bit important. Fig. 9 depicts the effective Young's modulus convergence following the longitudinal direction as the REV size rises. This effective elastic property is unstable on the first volumes. After the sixth volume, it becomes stable since these volumes can be considered Representative. This successful convergence test permits us to consider this REV size reasonably good for spruce. Notably, the transverse values of spruce evolve in a quasi-similar way. However, since poplar is presented here as one example of a dual-porosity organization (vessel lumens and fiber lumens), its convergence is open to question.

We have just assured the convergence behavior of spruce along the longitudinal direction (L). The aim is devoted to surveying the effects of the selected sizes of the REV on the macroscopic mechanical properties of some wood species by carrying out a series of homogenization analysis. The focus will be on the convergence of the porosity from spruce, poplar, and maple wood by increasing the REV size in the transverse plane (R,T). To that purpose, the REV has to be representative of porosity. A configuration on each considered REV for these species with sufficiently suitable size is given by,

$$\begin{aligned} \text{REV}_i &= [x_0 - i\Delta x, x_0 + i\Delta x] \times [y_0 - i\Delta y, y_0 + i\Delta y] \times [z_0 - \Delta z, z_0 + \Delta z], \\ i &= 1, \dots, 10. \end{aligned} \tag{17}$$

The step following the longitudinal direction is fixed for each wood sample, i.e., $\Delta z = 3$. Normally, the geometrical center (x_0, y_0, z_0) of the REV is fixed, but it is modified in some cases to capture many vessels. This concerns the smallest element size for poplar and maple samples. After each test, the volume of the REV is concurrently raised in the radial and tangential directions following the uniform steps $\Delta x = \Delta y = 32$. Tab. 3 reports the identified values of the macroscopic properties via the computational homogenization of the spruce, poplar, and maple species along the radial and tangential directions: This table summarizes the main results of this work. From this set of values, we obtained a data set that gave each sample the macroscopic Young's modulus as a function of the REV size for the various solid fractions obtained by the mesher. Fig. 10 depicts the convergence trends associated with changing REV sizes for the considered samples. As in previous convergence, the homogenized elasticity property is sensitive in the first volume of this series size. It can be seen from this figure that all the homogenized values become close to each other as the REV size increases. This result agrees with the strong and successful convergence test. This convergence is noted in the last volumes as the size of REV is sufficiently large. Since the

shape of vessels for both poplar and maple species is extended in the radial direction, the macroscopic transverse properties show a notable difference between them. This difference is much more significant compared to the spruce wood.

In light of Tab. 3, the predicted simulations were performed in the two transverse directions of wood (radial and tangential). The predicted macroscopic values are higher in the radial direction than in the tangential direction for all samples, including the intermediate spruce species. The cellular morphology used here for the intermediate wood differs from other species. However, its solid fraction corresponds more closely to the poplar and maple ones, consequently justifying the interesting outputs. It is clearly seen that the macroscopic mechanical properties depend strongly on the porosity fraction and morphological species. It is explained by acting the solid components on the model at different spatial scales. Note that the convergence has reached a rapid level for the spruce compared to other species.

The mechanical behavior of two wood tissues, poplar and maple specimens, was simulated using the FE method in both the radial and tangential directions. The FE modeling and analytical analysis of energy stress in the microstructure was performed for validation and confirmed the convergence results. This analysis also contributes to the mechanical response, as described in many works [81, 82]. Sretenovic et al. [81] investigate the stress transfer from the matrix material to reinforce discontinuous fibers for a wide range of composite materials. For the same purpose, the mechanism of stress transfer has been studied in [82], when the wood is embedded in a polymer matrix to provide a general understanding of its mechanical properties and microscale deformation process. Fig. 11 depicts the transfer properties of the wood species. To clarify this transfer, we adopt a strategy that assumes two REV types can be chosen. The figure is shared into two lines in which the minimal REV presented in the top diagrams is of $192 \times 192 \times 6$ voxels, while the maximal REV presented in the bottom diagrams is of $640 \times 640 \times 6$ voxels. We can see in the top diagrams that the energy grew radially from the left side and gradually extended to the right side of the sample. The same behavior was observed in the bottom diagrams. The energy spreads from the top to the bottom, following the tangential direction. We report that the energy transfer stays valid tangentially for the smallest domain size that complies with the minimum REV size, and radially for well-distributed pores across the microstructure with the maximum REV size. Note that the size of the REV varies spatially and depends on the presented quantity. A better largely quantitative of the REV size compared to the dimension of pores satisfies convergence. This occurs for the selected specimens since they have the considerable variability in vessel dimensions compared to the spruce species. The presented simulations are consistent with our visual observation, mainly, there is a relationship between the domain size and convergence.

The framework's straightforward application is illustrated in Fig. 11, which shows the formation and development of a stress transfer zone across the microstructure. In all simulation tests, a great variety of high stresses is observed. The red color scales the higher values, whereas the blue color presents the lower values. At first sight, the value of this stress transfer depends on the loading direction. Again, following this analysis, the simulated stress transfer resulting from the FE model demonstrated a good agreement. The transfer starts

forming energy zones, increasing this energy from the contact zone, where the stress force is enforced, until the end zone, where it is free. Under these radial (respectively tangential) loading conditions, the transfer propagates so that the radial (respectively tangential) stress always has higher values. In this case, when the radial component is excessive, the tangential component is low, and vice versa. In the same situation, as the load is increased, the radial transfer will be much more important, and the tangential transfer will be reduced significantly.

In what follows, we will carry out several numerical simulations to achieve the validation of the prediction approach by the framework. The homogenization approaches discussed below yield the estimated macroscopic elastic properties from the microscopic structure of heterogeneous materials. Indeed, the microscopic characterization at each tetrahedral cell scale is a necessary step that allows to anticipate the material's macroscopic behavior. Generally, the homogenized model regarded as a two-phase made up of gas brick embedded in a connected solid phase provides the effective transverse modulus E^h expressed as follows:

$$\frac{1}{E_{Series}^h} = \frac{\alpha_g}{E_{Eff}^g} + \frac{\alpha_s}{E_{Eff}^s}, E_{Parallel}^h = \alpha_g E_{Eff}^g + \alpha_s E_{Eff}^s. \quad (18)$$

This novel parallel-series model consisting of a series model and a parallel model is introduced, to compute the averaged mechanical constants in transverse plane from the averaged stiffness matrix $\bar{\mathbf{C}}$ introduced previously by the relationship (11). This model given by (18) is formulated in terms of E_{Eff}^g , E_{Eff}^s , α_g , and α_s which are the effective Young's modulus and volume fraction for gas and solid respectively, while the subscripts g and s indicate the phase for gas and solid states respectively. Since the choice of a homogenization scheme to model the wood material depends on its microstructure, the poplar, spruce, and maple wood specimens are investigated. In addition to the intermediate spruce specimen treated through this paper, the earlywood and latewood are considered here to present much variability among wood species. The aim is to enrich this investigation by varying the solid fraction. The analysis of the dimensionless equivalent elasticity leads to illustrate the advantages of the proposed specimens. The present homogenization technique provides the transition of earlywood and latewood information. In particular, its minimal and maximal solid fractions indicate the capability of determining the transition using these specimens. The literature [83, 84, 85] offers several contributions concerning the distinction between earlywood and latewood regarding their homogenized properties. From these specimens, a homogenization strategy of only the solid phase is proposed to describe the mechanical and physical properties of macroscopic structures with heterogeneous microstructures. This proposed homogenization is based on the assumption that micro-stress/micro-strain distribution is homogeneous in the solid matrix. We refer to the macroscopic and microscopic stress measures $\bar{\sigma}$ and σ , and their associated work-conjugate strains $\bar{\varepsilon}$ and ε in subsection 2.3.

A series of mechanical uniaxial traction and compression tests of invoked material samples are carried out to determine the homogenized Young's moduli. During these tests, the lateral faces remain blocked to capture much-averaged values. However, the face in where the force is applied stays free for the mechanical uniaxial testing. The mean homogenized Young's

moduli E_R^h , E_T^h , and E_L^h are determined following respectively the radial, tangential, and longitudinal directions. In this study, the REV microstructures are presented with large voxel size. The real brick specimens in three-dimensional space are chosen in such a way as to cover different values of solid fractions. The significant reference of volume subjects to good precision of macroscopic components. Following the procedure established above, the effective elastic properties of one single-phase microstructures without pores are obtained. Fig. 12 provides these results for various microstructures realizations that are presented in terms of volume fractions. First, it can legibly be seen that the REVs with greater volumic fraction have bigger radial and tangential Young's moduli. The effective Young's moduli E_L^h has much higher values locations compared to homogenized Young's moduli E_R^h and E_T^h as shown in Figs. 12a-12b. These radial and tangential averaged values have a declined tendency of effective material properties due to the influence of material properties uncertainties. The radial Young's moduli E_R^h are higher than the tangential Young's moduli E_T^h for all the wood species. Note that the macroscopic value is very close to the series model concerning the spruce earlywood. However, the value becomes close to the parallel model for the spruce latewood. The anisotropic ratio is inverted if the porosity is dilated slightly for these specimens. In this situation, it becomes the opposite due to the morphological reasons and connected phase. Mainly, it is caused of the flattened cells. This means the solid fraction is augmented by around 0.2 for these specimens. Then, the effective elastic modulus is lower in the radial direction than in the tangential direction. These supply results even obtained and not presented here; confirm those obtained by Perré et al. [86] for thermal/mass diffusivity and mechanical properties of the real wood tissue structure.

The consistency of survey estimates the macroscopic values following the longitudinal direction is examined as follows. Figs. 12c-12d illustrate the effective macroscopic values E_L^h corresponding approximately to the fundamental parallel model. If these values are exactly the same as the parallel model, then it means that the obtained result can be false. Nevertheless, this approximation is a great sign of conformity result. Generally, these results show consistency concerning our macroscopic numerical predictions of the homogenization aspect. It confirms the capacity framework to forecast the homogenized elastic properties using the FE method.

3.3 Heterogeneity overview of wood

This work aims to develop a realistic heterogeneous micromechanical model of wood by taking into account its microstructures in two regions and applying this model to analyze the effect of wood microstructure on the homogenization aspect. In this regard, the numerical homogenization technique is used to estimate the effective physical properties of dual-phase heterogeneous wood materials [87, 88]. The mechanical computational leads bring out the influence of the porosity on the physical properties. This is achieved using two different homogeneous materials. The global microstructure and composition are examined heterogeneous, where each phase is homogeneous with uniform characteristics. The physical characteristics affecting the solid structure are preserved, as described in part 2.2. Recalling that cellulose and hemicellulose are the two fundamental constituents of wood at

the ultrastructural scale. These constituents presented by the second phase are treated as an equivalent material and subjected to 2% for the solid elastic properties. Note that many research works [89, 90, 91, 92] have explored the relationship between microstructure with heterogeneous multiple layers and mechanical properties in cellulose-based materials. For instance, a multiscale mechanic framework for analyzing the elastic properties of densified wood, considering its chemical component, is developed in [89, 90] using analytical and FE approaches. Additionally, the aim of the investigations [91, 92] is to study the mechanical properties of cellulose interactions on the anisotropic structure in food and medical applications. Due to the complex imbrication of structural parameters on wood elasticity, our feature of the 2% chain composition leads to simplifying and highlighting the generality of the heterogeneity procedure.

Previously, the classical homogeneous model provided a clear and comprehensive overview of the importance and impact of treating the local wood properties. The heterogeneity approach is useful for understanding which structural parameters control the material properties, such as the realistic stiffness and failure analysis. The mechanical behavior of the anisotropy and heterogeneity (Fig. 13) was simulated using our FE framework in both the radial and tangential directions. Running heterogeneous wood material is time-consuming and consists of tensile and compression tests at small deformations scale. The investigated materials, such as the poplar and maple species, with regularities in the cell shape and large sizes. Because meshes made with interconnecting pores are required via porous meshes. The FE framework is extended so that the effect of material heterogeneity is explored within the possibilities offered by this model. The effect of wood microstructures on its elastic properties was studied within the systematic computational modeling. In our studies, this model will be used to predict the wood response while mechanical loading is applied. The same figure shows two exhibit diagrams covering the stress tensor at each material point under tensile loading conditions applied to the REV. This contribution establishes a transfer of tensorial stress data, radially and tangentially, respectively, in the left and right diagrams. This result is consistent with the energy transfer illustrated in Fig. 11. The ultimate stress with higher values evolves radially when a tensile force is applied in this direction, and vice versa while following another direction. The improved framework contributes through porous structure a weakly mechanical energy during the deformation. From a physical point of view, one must expect to obtain a smoother response, rather than this non-variability. This is explained by attributing the low mechanical properties and other characteristics of the pore structure.

We believe that the present framework can provide further investigations on complex heterogeneous wood materials. More numerical simulations are demanded to provide information on the basic constituents. The homogenization-based multi-scale techniques are adopted to physically treat the intricate mechanisms of wood at the macroscopic level. The results provided by the homogeneous and heterogeneous wood materials via the FE method are performed on a suitable REV [93]. A series-parallel mixture model via relation (18) is proposed to predict the overall property. As shown in Fig. 13, the two elastic materials are connected together in parallel to form the investigated wood material. To further understand the effect of cellulose components on the mechanical properties of wood, we

have compared the average tensile Young’s modulus along the anisotropic direction (Fig. 14). To this aim, recall that the overall Young’s modulus is the average of the moduli of the constituents weighted by the volume fraction of each phase [94, 95, 96]. The assumed porosity highly influences the prediction of effective properties in the case of heterogeneous against the homogeneous framework [97, 98, 99]. First, it can clearly be seen that the REVs with greater porosities have smaller predictive effective elastic properties that must remain in the physical ranges. At the same time, the radial Young’s moduli E_R^h are greater than the tangential Young’s moduli E_T^h for all heterogeneous samples. This remark is expanded for the spruce specimen. As expected, the radial and tangential heterogeneous homogenized Young’s moduli E_R^h and E_T^h are markedly greater than homogeneous ones. The wood cellulose effect demonstrates superior performance over homogeneous, so practically, higher values indicate better mechanical properties of heterogeneous materials. We conclude that the results obtained via the presented methodology with the FE tool yields simulate any wood microstructure with great accuracy [100, 101, 102].

4 Discussion and concluding remarks

The wood elements are still known for multi-scale and anisotropic aspects. The scientific interest of this work consists of understanding the wood microstructures utilizing the X-ray tomography technique. This technique is based on scan parameters with specific environmental conditions to access their real morphology. The poplar, spruce, and maple wood specimens with representative dimensions are scanned using the tomograph and analyzed. Next, image processing is carried out to provide these samples 3D digital morphology. The aim is to use this representation to generate a 3D unstructured mesh that is the necessary input data for the finite element method (FEM) framework.

In the scope of computer science, we have shown that the FEM is the numerical procedure that aims to describe the physical structure in a three-dimensional space, respecting the mathematical approach. This framework of FEM was consistent with the structure topologies of different phases species. The mechanical model of the 3D real structure has been further validated, through numerical procedure. Particularly, the numerical results highlight the effect of wood’s anisotropy at the microscopic scale. The higher mechanical properties of these tested samples are presented by showing the stress-strain curves. The summarized results for each sample provide a very realistic microstructure deformation.

The solving linear system in parallel was implemented to exemplify the improvement of the computational efficiency and speed of the code on the computer architecture. Indeed, the post-processing of mechanical modelling of these microstructures can be very time consuming. The coefficient of the global matrix is presented in a sparse format, which makes this method more accurate in performing small deformation scales. We would like to show that the parallel computing using Message Passing Interface (MPI), and Compute Unified Device Architecture (CUDA), can greatly rise the computational efficiency of modelling framework. The presented work will be extended for multi-scale simulation of 3D fiber-reinforced composite modelling. Then we will investigate the influence of fiber distribution

on the simulation, in which multiple fibers with different orientations are presented. We will carry out experimental tests using universal testing machine. The studied specimens with fiber will be placed in this machine according to the standard of these structures.

CRedit authorship contribution statement

Tarik Chakkour: Conceptualization; Methodology; Validation; Formal analysis; Investigation; Data Curation Management; Writing-Original Draft; Visualization. **Patrick Perré:** Conceptualization; Methodology; Formal analysis; Investigation; Resources; Data Curation Management; Writing-Review and Editing; Supervision; Project administration; Funding acquisition.

Declaration of competing interest

The authors declare that they have no known competing financial interests or personal relationships that could have appeared to influence the work reported in this paper.

Availability of data

Data will be made available on request.

Consent to participate

All authors contributed to this work. All authors read and approved the final manuscript.

Acknowledgements:

First, the authors also adress many thanks to the anonymous reviewers for their helpful and valuable comments that have greatly improved the paper. This study was carried out in the Centre Européen de Biotechnologie et de Bioéconomie (CEBB), supported by the Région Grand Est, Département de la Marne, Greater Reims and the European Union. In particular, the authors would like to thank the Département de la Marne, Greater Reims, Région Grand Est and the European Union along with the fund (FEDER Grand Est 2021-2027) for their financial support of the Chair of Biotechnology of CentraleSupélec.

References

- [1] J. Wang, X. Han, W. Wu, X. Wang, L. Ding, Y. Wang, S. Li, J. Hu, W. Yang, C. Zhang, et al., Oxidation of cellulose molecules toward delignified oxidated hot-pressed wood with improved mechanical properties, *International Journal of Biological Macromolecules* 231 (2023) 123343.
- [2] M. Chutturi, S. Gillela, S. M. Yadav, E. S. Wibowo, K. Sihag, S. M. Rangppa, P. Bhuyar, S. Siengchin, P. Antov, L. Kristak, et al., A comprehensive review of the synthesis strategies, properties, and applications of transparent wood as a renewable and sustainable resource, *Science of The Total Environment* 864 (2023) 161067.
- [3] S. M. Koch, C. Goldhahn, F. J. Muller, W. Yan, C. Pilz-Allen, C. M. Bidan, B. Ciabattoni, L. Stricker, P. Fratzl, T. Keplinger, et al., Anisotropic wood-hydrogel composites: Extending mechanical properties of wood towards soft materials' applications, *Materials Today Bio* 22 (2023) 100772.
- [4] Y. Chen, L. Zhang, C. Mei, Y. Li, G. Duan, S. Agarwal, A. Greiner, C. Ma, S. Jiang, Wood-inspired anisotropic cellulose nanofibril composite sponges for multifunctional applications, *ACS applied materials & interfaces* 12 (31) (2020) 35513–35522.
- [5] S. He, X. Zhao, E. Q. Wang, G. S. Chen, P.-Y. Chen, L. Hu, Engineered wood: Sustainable technologies and applications, *Annual Review of Materials Research* 53 (2023).
- [6] P. Niemz, M. Dunky, Bonding of solid wood-based materials for timber construction, *Biobased Adhesives: Sources, Characteristics and Applications* (2023) 621–658.
- [7] T. Chakkour, Reengineering of aerodynamic flow-field module, *Engineering Mathematics Letters* 2018 (Article ID 4) (2018) [http-scik](http://scik).
- [8] J. Wang, D. Zhang, F. Chu, Wood-derived functional polymeric materials, *Advanced Materials* 33 (28) (2021) 2001135.
- [9] Y. Zuo, J. Feng, T.-O. Soyol-Erdene, Z. Wei, T. Hu, Y. Zhang, W. Tang, Recent advances in wood-derived monolithic carbon materials: Synthesis approaches, modification methods and environmental applications, *Chemical Engineering Journal* 463 (2023) 142332.
- [10] F. Aldakheel, E. S. Elsayed, T. I. Zohdi, P. Wriggers, Efficient multiscale modeling of heterogeneous materials using deep neural networks, *Computational Mechanics* (2023) 1–17.
- [11] R. Yazdanparast, R. Rafiee, Determining in-plane material properties of square core cellular materials using computational homogenization technique, *Engineering with Computers* 39 (1) (2023) 373–386.

- [12] J. Liu, W. Liu, R. Tan, W. Huang, B. Wang, S. Zhang, M. Zhang, Drying strain behavior of elm earlywood and latewood with digital image correlation method, *Drying Technology* 41 (5) (2023) 746–753.
- [13] A. Liszka, R. Wightman, D. Latowski, M. Bourdon, K. B. Krogh, J. J. Lyczakowski, Structural differences of cell walls in earlywood and latewood of *pinus sylvestris* and their contribution to biomass recalcitrance, *Frontiers in Plant Science* 14 (2023) 1283093.
- [14] G. K. Zelenov, L. V. Belokopytova, E. A. Babushkina, D. F. Zhirnova, B. Yang, X. Peng, J. Liu, G. A. Sitnikov, E. A. Vaganov, Reconstruction of seasonal kinetics in conifer radial growth from daily meteorological conditions, tree-ring width, and radial size of tracheids, *Forests* 15 (2) (2024) 249.
- [15] X. Zhang, H. Liu, T. Rademacher, Higher latewood to earlywood ratio increases resistance of radial growth to severe droughts in larch, *Science of The Total Environment* 912 (2024) 169165.
- [16] J. J. Camarero, X. Serra-Maluquer, M. Colangelo, A. Gazol, M. Pizarro, Latewood intra-annual density fluctuations indicate wet summer conditions and enhanced canopy activity in a mediterranean ring-porous oak, *IAWA Journal* 1 (aop) (2023) 1–14.
- [17] A. Słupianek, E. Myśkow, A. Kasprowicz-Maluśki, A. Dolzblasz, R. Żytkowiak, M. Turzańska, K. Sokołowska, Seasonal dynamics of cell-to-cell transport in angiosperm wood, *Journal of Experimental Botany* (2023) erad469.
- [18] Ü. Büyüksarı, N. As, T. Dündar, Mechanical properties of earlywood and latewood sections of scots pine wood, *BioResources* 12 (2) (2017) 4004–4012.
- [19] W. Li, Z. Zhang, C. Mei, P. Kibleur, J. Van Acker, J. Van Den Bulcke, Understanding the mechanical strength and dynamic structural changes of wood-based products using x-ray computed tomography, *Wood Material Science & Engineering* (2022) 1–10.
- [20] R. Lehnebach, M. Campioli, J. Gričar, P. Prislan, B. Mariën, H. Beeckman, J. Van den Bulcke, High-resolution x-ray computed tomography: a new workflow for the analysis of xylogenesis and intra-seasonal wood biomass production, *Frontiers in plant science* 12 (2021).
- [21] J. L. Paris, F. A. Kamke, Quantitative wood–adhesive penetration with x-ray computed tomography, *International Journal of Adhesion and Adhesives* 61 (2015) 71–80.
- [22] X. Zhang, B. Xiao, H. Andrä, Z. Ma, Multiscale modeling of macroscopic and microscopic residual stresses in metal matrix composites using 3d realistic digital microstructure models, *Composite Structures* 137 (2016) 18–32.
- [23] S. Dai, P. Cunningham, Multi-scale damage modelling of 3d woven composites under uni-axial tension, *Composite Structures* 142 (2016) 298–312.

- [24] A. Catapano, M. Montemurro, A multi-scale approach for the optimum design of sandwich plates with honeycomb core. part i: homogenisation of core properties, *Composite structures* 118 (2014) 664–676.
- [25] K. Spanos, S. Georgantzinos, N. Anifantis, Mechanical properties of graphene nanocomposites: A multiscale finite element prediction, *Composite Structures* 132 (2015) 536–544.
- [26] Z. Wang, T. Wang, W. Wang, Z. Zhang, Size of representative elementary volume for heterogeneous rocks evaluated using distinct element method, *Acta Geotechnica* 18 (4) (2023) 1883–1900.
- [27] S. Aney, A. Rege, The effect of pore sizes on the elastic behaviour of open-porous cellular materials, *Mathematics and Mechanics of Solids* 28 (7) (2023) 1624–1634.
- [28] C. González, J. LLorca, Mechanical behavior of unidirectional fiber-reinforced polymers under transverse compression: Microscopic mechanisms and modeling, *Composites Science and Technology* 67 (13) (2007) 2795–2806.
- [29] L. Riaño, L. Belec, Y. Joliff, Validation of a representative volume element for unidirectional fiber-reinforced composites: Case of a monotonic traction in its cross section, *Composite Structures* 154 (2016) 11–16.
- [30] S. Balay, S. Abhyankar, M. Adams, J. Brown, P. Brune, K. Buschelman, L. Dalcin, A. Dener, V. Eijkhout, W. Gropp, et al., *Petsc users manual* (2019).
- [31] Y. Saad, *Sparskit: a basic tool kit for sparse matrix computations* (1994).
- [32] S. L. Wood, K. Jacobson, W. T. Jones, W. K. Anderson, Sparse linear algebra toolkit for computational aerodynamics, in: *AIAA Scitech 2020 Forum*, 2020, p. 0317.
- [33] M. Othman, Nonlinear time-domain finite element solver for quantum information science applications, *Bulletin of the American Physical Society* (2024).
- [34] W.-L. Feng, J. Zhong, T. Chen, X.-F. Yuan, Scalability of viscoelastic fluid solvers based on openfoam-petsc framework in large-scale parallel computing, in: *Journal of Physics: Conference Series*, Vol. 2610, IOP Publishing, 2023, p. 012012.
- [35] Z. Wang, T. A. Palmer, A. M. Beese, Effect of processing parameters on microstructure and tensile properties of austenitic stainless steel 304l made by directed energy deposition additive manufacturing, *Acta Materialia* 110 (2016) 226–235.
- [36] M. Z. Ahmed, K. Chadha, S. Reddy, D. Shahriari, P. P. Bhattacharjee, M. Jahazi, Influence of process parameters on microstructure evolution during hot deformation of a eutectic high-entropy alloy (eha), *Metallurgical and Materials Transactions A* 51 (12) (2020) 6406–6420.

- [37] H. Yue, Y. Chen, X. Wang, F. Kong, Effect of beam current on microstructure, phase, grain characteristic and mechanical properties of ti-47al-2cr-2nb alloy fabricated by selective electron beam melting, *Journal of Alloys and Compounds* 750 (2018) 617–625.
- [38] R. T. Mills, M. F. Adams, S. Balay, J. Brown, A. Dener, M. Knepley, S. E. Kruger, H. Morgan, T. Munson, K. Rupp, et al., Toward performance-portable petsc for gpu-based exascale systems, *Parallel Computing* 108 (2021) 102831.
- [39] J. D. Trotter, J. Langguth, X. Cai, Targeting performance and user-friendliness: Gpu-accelerated finite element computation with automated code generation in fenics, *Parallel Computing* 118 (2023) 103051.
- [40] T. Chakkour, Parallel computation to bidimensional heat equation using mpi/cuda and fftw package, *Frontiers in Computer Science* 5 (2024). doi:10.3389/fcomp.2023.1305800.
- [41] T. Chakkour, High-quality implementation for a continuous-in-time financial api in c#, *Frontiers in Computer Science* 6 (2024). doi:10.3389/fcomp.2024.1371052.
- [42] V. Hapla, M. G. Knepley, M. Afanasiev, C. Boehm, M. van Driel, L. Krischer, A. Fichtner, Fully parallel mesh i/o using petsc dmpex with an application to waveform modeling, *SIAM Journal on Scientific Computing* 43 (2) (2021) C127–C153.
- [43] P. Jolivet, J. E. Roman, S. Zampini, Ksphpddm and pchpddm: Extending petsc with advanced krylov methods and robust multilevel overlapping schwarz preconditioners, *Computers & Mathematics with Applications* 84 (2021) 277–295.
- [44] M. A. Salazar de Troya, D. A. Tortorelli, Three-dimensional adaptive mesh refinement in stress-constrained topology optimization, *Structural and Multidisciplinary Optimization* 62 (5) (2020) 2467–2479.
- [45] J. Schindelin, I. Arganda-Carreras, E. Frise, V. Kaynig, M. Longair, T. Pietzsch, S. Preibisch, C. Rueden, S. Saalfeld, B. Schmid, et al., Fiji: an open-source platform for biological-image analysis, *Nature methods* 9 (7) (2012) 676–682.
- [46] C. A. Schneider, W. S. Rasband, K. W. Eliceiri, Nih image to imagej: 25 years of image analysis, *Nature methods* 9 (7) (2012) 671–675.
- [47] F. De Chaumont, S. Dallongeville, N. Chenouard, N. Hervé, S. Pop, T. Provoost, V. Meas-Yedid, P. Pankajakshan, T. Lecomte, Y. Le Montagner, et al., Icy: an open bioimage informatics platform for extended reproducible research, *Nature methods* 9 (7) (2012) 690–696.
- [48] N. Otsu, A threshold selection method from gray-level histograms, *IEEE transactions on systems, man, and cybernetics* 9 (1) (1979) 62–66.

- [49] C. A. Beretta, S. Liu, A. Stegemann, Z. Gan, L. Wang, L. L. Tan, R. Kuner, Quanty-cfos, a novel imagej/fiji algorithm for automated counting of immunoreactive cells in tissue sections, *Cells* 12 (5) (2023) 704.
- [50] E. Kugler, E.-M. Breitenbach, R. MacDonald, Glia cell morphology analysis using the fiji gliamorph toolkit, *Current Protocols* 3 (1) (2023) e654.
- [51] T. Chakkour, Finite element modelling of complex 3D image data with quantification and analysis, *Oxford Open Materials Science* 4 (1) (2024) itae003. [doi:10.1093/oxfmat/itae003](https://doi.org/10.1093/oxfmat/itae003).
- [52] C. Zhang, M. Chen, S. Keten, B. Coasne, D. Derome, J. Carmeliet, Hygromechanical mechanisms of wood cell wall revealed by molecular modeling and mixture rule analysis, *Science Advances* 7 (37) (2021) eabi8919.
- [53] C. Zhang, M. Chen, B. Coasne, S. Keten, D. Derome, J. Carmeliet, Hygromechanics of softwood cellulosic nanocomposite with intermolecular interactions at fiber-matrix interface investigated with molecular dynamics, *Composites Part B: Engineering* 228 (2022) 109449.
- [54] A. Alkadri, D. Jullien, O. Arnould, E. Rosenkrantz, P. Langbour, L. Hovasse, J. Gril, Hygromechanical properties of grenadilla wood (*dalbergia melanoxylon*), *Wood Science and Technology* 54 (5) (2020) 1269–1297.
- [55] P. Grönquist, P. Panchadcharam, D. Wood, A. Menges, M. Rüggeberg, F. K. Wittel, Computational analysis of hygromorphic self-shaping wood gridshell structures, *Royal Society open science* 7 (7) (2020) 192210.
- [56] R. C. Neagu, E. K. Gamstedt, Modelling of effects of ultrastructural morphology on the hydroelastic properties of wood fibres, *Journal of Materials Science* 42 (2007) 10254–10274.
- [57] N. Charupeng, P. Kunthong, A novel finite element algorithm for predicting the elastic properties of wood fibers, *International Journal of Computational Materials Science and Engineering* 11 (01) (2022) 2150027.
- [58] M. Stucu, A recursive concentric cylinder model for composites containing coated fibers, *International Journal of Solids and Structures* 29 (2) (1992) 197–213.
- [59] A. Düster, J. Parvizián, Z. Yang, E. Rank, The finite cell method for three-dimensional problems of solid mechanics, *Computer methods in applied mechanics and engineering* 197 (45-48) (2008) 3768–3782.
- [60] X. Shen, Y. Xue, Q. Yang, S. Zhu, Finite element method coupling penalty method for flexural shell model, *Adv. Appl. Math. Mech* 14 (2) (2022) 365–385.

- [61] Z. Yu, Y. Cui, Q. Zhang, J. Liu, Y. Qin, Thermo-mechanical coupled analysis of v-belt drive system via absolute nodal coordinate formulation, *Mechanism and Machine Theory* 174 (2022) 104906.
- [62] B. Zheng, T. Li, H. Qi, L. Gao, X. Liu, L. Yuan, Physics-informed machine learning model for computational fracture of quasi-brittle materials without labelled data, *International Journal of Mechanical Sciences* 223 (2022) 107282.
- [63] W. Wang, Y. Wu, H. Wu, C. Yang, Q. Feng, Numerical analysis of dynamic compaction using fem-sph coupling method, *Soil Dynamics and Earthquake Engineering* 140 (2021) 106420.
- [64] T. Zhu, S. Atluri, A modified collocation method and a penalty formulation for enforcing the essential boundary conditions in the element free galerkin method, *Computational Mechanics* 21 (3) (1998) 211–222.
- [65] M. Königsberger, M. Lukacevic, J. Füssl, Multiscale micromechanics modeling of plant fibers: upscaling of stiffness and elastic limits from cellulose nanofibrils to technical fibers, *Materials and Structures* 56 (1) (2023) 13.
- [66] M. Königsberger, V. Senk, M. Lukacevic, M. Wimmer, J. Füssl, Micromechanics stiffness upscaling of plant fiber-reinforced composites, *Composites Part B: Engineering* 281 (2024) 111571.
- [67] Z. Guo, X. Liu, L. Huang, S. Adhikari, X. Liang, Analytical homogenization for equivalent in-plane elastic moduli of prestressed lattices based on the micropolar elasticity model, *Composite Structures* (2024) 118391.
- [68] J.-F. Ganghoffer, A. Wazne, H. Reda, Frontiers in homogenization methods towards generalized continua for architected materials, *Mechanics Research Communications* 130 (2023) 104114.
- [69] M. Tonutti, G. Gras, G.-Z. Yang, A machine learning approach for real-time modelling of tissue deformation in image-guided neurosurgery, *Artificial intelligence in medicine* 80 (2017) 39–47.
- [70] G. M. Della Pepa, G. Menna, V. Stifano, A. M. Pezzullo, A. M. Auricchio, A. Rapisarda, V. M. Caccavella, G. La Rocca, G. Sabatino, E. Marchese, et al., Predicting meningioma consistency and brain-meningioma interface with intraoperative strain ultrasound elastography: a novel application to guide surgical strategy, *Neurosurgical Focus* 50 (1) (2021) E15.
- [71] N. H. Hart, S. Nimphius, T. Rantalainen, A. Ireland, A. Siafarikas, R. Newton, Mechanical basis of bone strength: influence of bone material, bone structure and muscle action, *Journal of musculoskeletal & neuronal interactions* 17 (3) (2017) 114.

- [72] P. Zioupos, H. O. Kirchner, H. Peterlik, Ageing bone fractures: The case of a ductile to brittle transition that shifts with age, *Bone* 131 (2020) 115176.
- [73] I. Gitman, H. Askes, L. Sluys, Representative volume: Existence and size determination, *Engineering fracture mechanics* 74 (16) (2007) 2518–2534.
- [74] R. Hill, Elastic properties of reinforced solids: some theoretical principles, *Journal of the Mechanics and Physics of Solids* 11 (5) (1963) 357–372.
- [75] D. Savvas, G. Stefanou, M. Papadrakakis, Determination of rve size for random composites with local volume fraction variation, *Computer Methods in Applied Mechanics and Engineering* 305 (2016) 340–358.
- [76] X. Tu, A. Shahba, J. Shen, S. Ghosh, Microstructure and property based statistically equivalent rves for polycrystalline-polyphase aluminum alloys, *International Journal of Plasticity* 115 (2019) 268–292.
- [77] S. Bernaud, I. Ramière, G. Latu, B. Michel, Pleiades: A numerical framework dedicated to the multiphysics and multiscale nuclear fuel behavior simulation, *Annals of Nuclear Energy* 205 (2024) 110577.
- [78] F. Freddi, L. Mingazzi, Adaptive mesh refinement for the phase field method: A fenics implementation, *Applications in Engineering Science* 14 (2023) 100127.
- [79] G. Liu, W. Huang, N. Leng, P. He, X. Li, M. Lin, Z. Lian, Y. Wang, J. Chen, W. Cai, Comparative biomechanical stability of the fixation of different miniplates in restorative laminoplasty after laminectomy: A finite element study, *Bioengineering* 11 (5) (2024) 519.
- [80] B. Mazian, E.-H. Quenjel, P. Perré, Thermal conductivity of the cell wall of wood predicted by inverse analysis of 3d homogenization, *International Journal of Heat and Mass Transfer* 217 (2023) 124700.
- [81] A. Sretenovic, U. Müller, W. Gindl, Mechanism of stress transfer in a single wood fibre-ldpe composite by means of electronic laser speckle interferometry, *Composites Part A: applied science and manufacturing* 37 (9) (2006) 1406–1412.
- [82] E. Jungstedt, C. Montanari, S. Östlund, L. Berglund, Mechanical properties of transparent high strength biocomposites from delignified wood veneer, *Composites Part A: Applied Science and Manufacturing* 133 (2020) 105853.
- [83] L. Melzerová, L. Kucíková, T. Janda, M. Šejnoha, et al., Estimation of orthotropic mechanical properties of wood based on non-destructive testing, *Wood Research* 61 (6) (2016) 861–870.

- [84] M. Šejnoha, L. Kucíková, J. Vorel, J. Sýkora, W. De. Wilde, Effective material properties of wood based on homogenization, *International Journal of Computational Methods and Experimental Measurements* 7 (2) (2019) 167–180.
- [85] A. Rafsanjani, D. Derome, F. K. Wittel, J. Carmeliet, Computational up-scaling of anisotropic swelling and mechanical behavior of hierarchical cellular materials, *Composites Science and Technology* 72 (6) (2012) 744–751.
- [86] P. Perré, G. Almeida, M. Ayouz, X. Frank, New modelling approaches to predict wood properties from its cellular structure: image-based representation and meshless methods, *Annals of Forest Science* 73 (2016) 147–162.
- [87] Y. Wang, G. Han, X. Liu, Y. Ren, H. Jiang, Flexural behaviors and failure mechanisms of cfrp sandwich structures with enhanced dual-phase lattice cores, *Composite Structures* 328 (2024) 117724.
- [88] C. Organista, R. Tang, Z. Shi, K. Jefimovs, D. Josell, L. Romano, S. Spindler, P. Kibleur, B. Blykers, M. Stampanoni, et al., Implementation of a dual-phase grating interferometer for multi-scale characterization of building materials by tunable dark-field imaging, *Scientific Reports* 14 (1) (2024) 384.
- [89] R. Song, F. Deng, X. Liang, J. Song, S. Shen, T. Li, A multiscale mechanics model for elastic properties of densified wood, *Journal of the Mechanics and Physics of Solids* 191 (2024) 105761.
- [90] N.-T. Phan, F. Auslender, J. Gril, R. Moutou Pitti, Effects of cellulose fibril cross-linking on the mechanical behavior of wood at different scales, *Wood Science and Technology* (2024) 1–29.
- [91] S.-Q. Chen, P. Lopez-Sanchez, D. Mikkelsen, M. Martinez-Sanz, Z. Li, S. Zhang, E. P. Gilbert, L. Li, M. J. Gidley, Hemicellulose-bacterial cellulose ribbon interactions affect the anisotropic mechanical behaviour of bacterial cellulose hydrogels, *Food Hydrocolloids* 136 (2023) 108283.
- [92] X. Lu, H. Jiao, Y. Shi, Y. Li, H. Zhang, Y. Fu, J. Guo, Q. Wang, X. Liu, M. Zhou, et al., Fabrication of bio-inspired anisotropic structures from biopolymers for biomedical applications: A review, *Carbohydrate Polymers* 308 (2023) 120669.
- [93] S. Okamoto, N. Akiyama, Y. Araki, K. Aoki, M. Inayama, Study on the strength of glued laminated timber beams with round holes: difference in structural performance between homogeneous-grade and heterogeneous-grade timber, *Journal of Wood Science* 67 (2021) 1–25.
- [94] S. Sugiman, S. Salman, M. Maryudi, Effects of volume fraction on water uptake and tensile properties of epoxy filled with inorganic fillers having different reactivity to water, *Materials Today Communications* 24 (2020) 101360.

- [95] Y. K. Galadima, W. Xia, E. Oterkus, S. Oterkus, A computational homogenization framework for non-ordinary state-based peridynamics, *Engineering with Computers* 39 (1) (2023) 461–487.
- [96] C. Naili, I. Doghri, T. Kanit, M. Sukiman, A. Aissa-Berraies, A. Imad, Short fiber reinforced composites: Unbiased full-field evaluation of various homogenization methods in elasticity, *Composites Science and Technology* 187 (2020) 107942.
- [97] Ravikant, V. K. Mittal, V. Gupta, Homogeneous and heterogeneous modeling of patient-specific hip implant under static and dynamic loading condition using finite element analysis, *Journal of The Institution of Engineers (India): Series D* 105 (1) (2024) 1–20.
- [98] H. A. Madkhali, M. Nawaz, S. O. Alharbi, Computational investigation of homogeneous-heterogeneous reactions in fluid with transport mechanisms: a finite element simulations approach, *Ain Shams Engineering Journal* 15 (3) (2024) 102449.
- [99] S. Yakupov, H. Kiyamov, N. Yakupov, I. Mukhamedova, A new variant of the fem for evaluation the strenght of structures of complex geometry with heterogeneous material structure, *Case studies in construction materials* 19 (2023) e02360.
- [100] J. Tao, P. Tahmasebi, M. A. Kader, D. Feng, M. Sahimi, P. D. Evans, M. Saadatfar, Wood biomimetics: Capturing and simulating the mesoscale complexity of willow using cross-correlation reconstruction algorithm and 3d printing, *Materials & Design* 228 (2023) 111812.
- [101] C.-W. Chang, C.-Y. Lin, H.-W. Kao, F.-C. Chang, Micromechanical analytical and inverse numerical modeling methods for determining the transverse elastic modulus of bamboo, *Wood Science and Technology* 57 (1) (2023) 75–92.
- [102] R. Bengtsson, M. Mousavi, R. Afshar, E. K. Gamstedt, Viscoelastic behavior of softwood based on a multiscale computational homogenization, *Mechanics of Materials* 179 (2023) 104586.

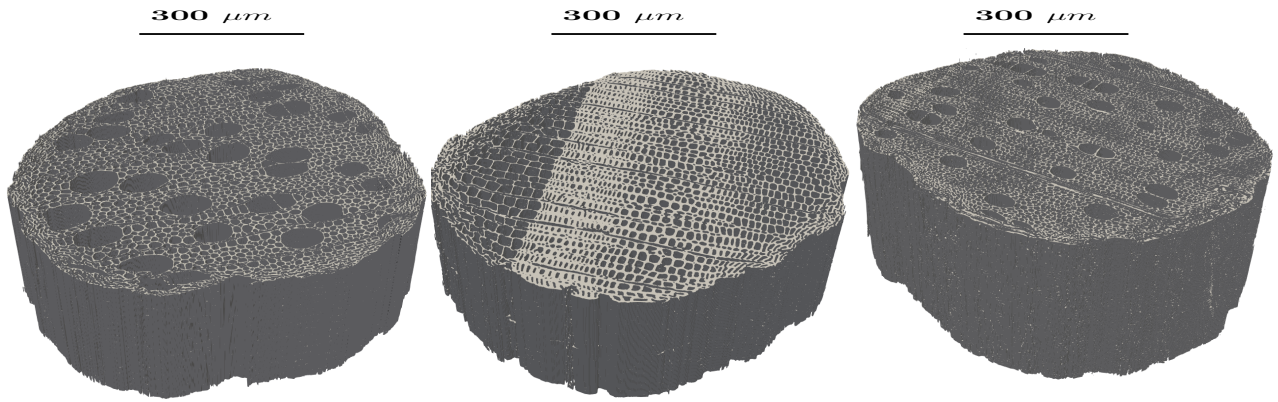


Figure 1: The 3D scanned samples of poplar (left), spruce (middle), and maple (right).

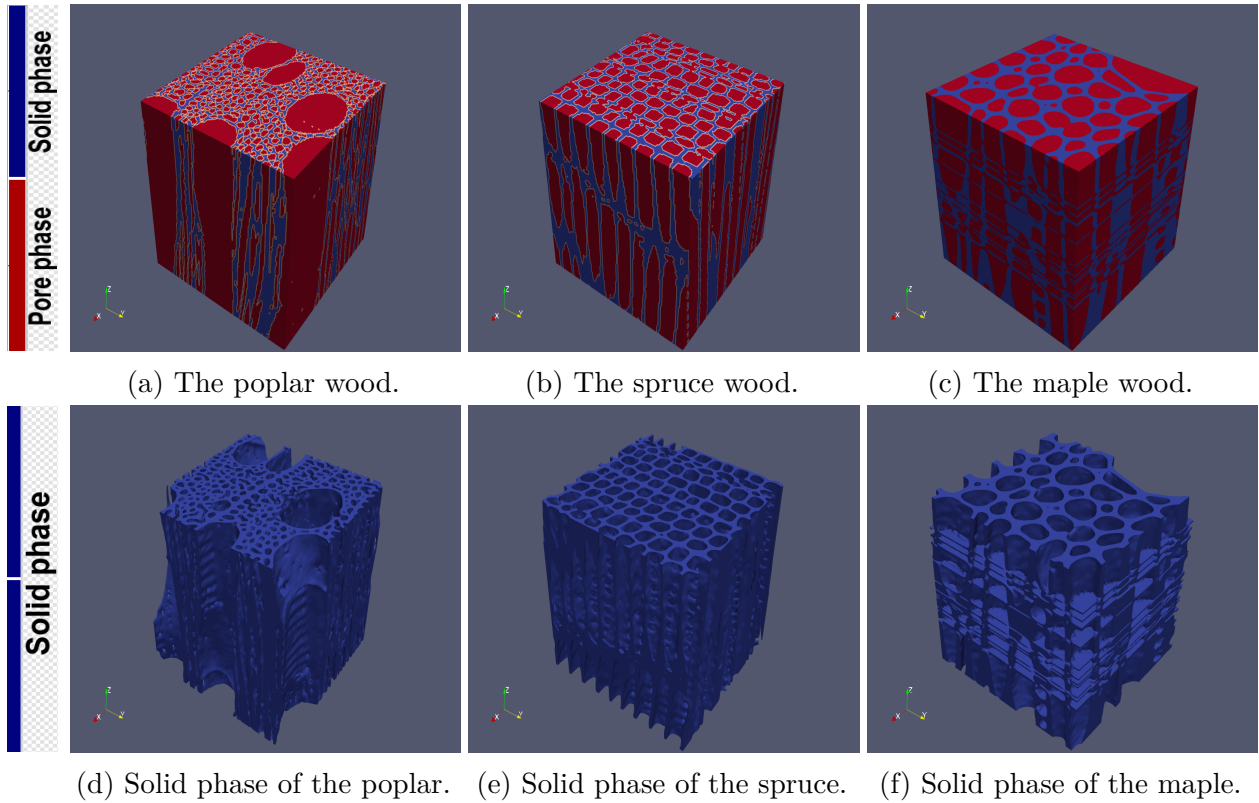


Figure 2: The extracted solid phase from the 3D reconstructed wood specimens scanned by X-ray nano-tomography presented in Fig. 1 to model the material microstructure. Each specimen having the same dimension $128 \times 128 \times 128$ voxels is treated with ImageJ-Python software.

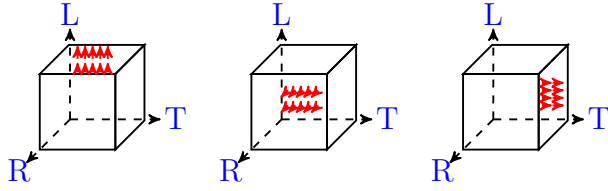


Figure 3: A 3D cubic material microstructure subjected to a uniform displacement on each particular face.

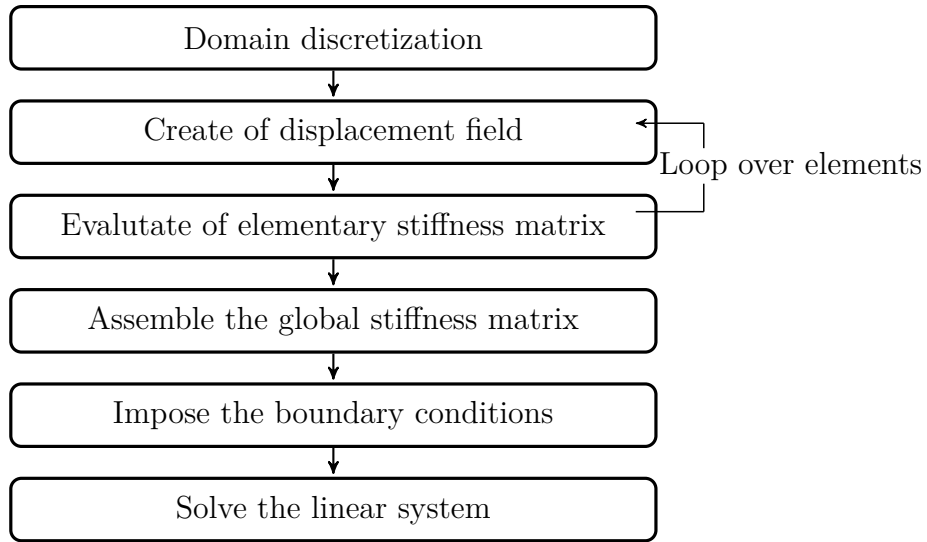


Figure 4: The computation process based on the homogenization scheme employing a FE discretization with displacement.

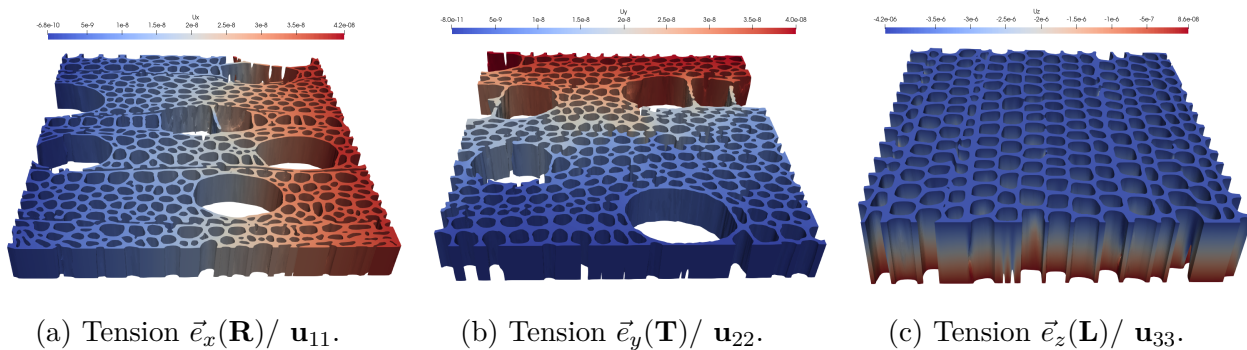
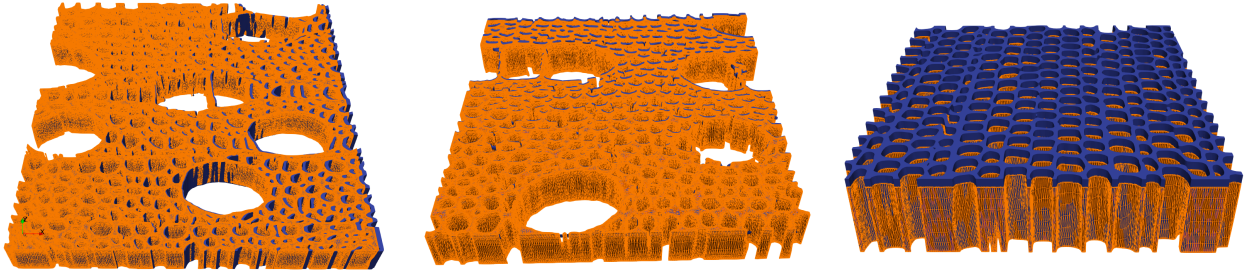


Figure 5: A series of mechanical tests demonstrating the validation of the orthotropic linear-elastic model for the poplar (left), maple (middle), and spruce (right) wood specimens. Each nodal displacement is generated for the uniaxial tensile test.



(a) Loading in the radial (**R**) direction. (b) Loading in the tangential (**T**) direction. (c) Loading in the longitudinal (**L**) direction.

Figure 6: Typical small deformation for the poplar (left), maple (middle), and spruce (right) wood specimens in each traction testing presented in Fig. 5. The original microstructure is presented in mesh by the orange color, while the deformed microstructure is presented by the blue color.

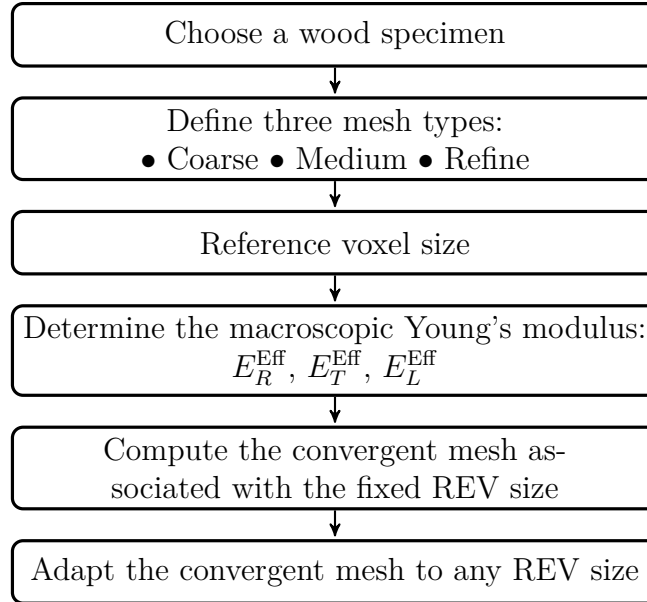
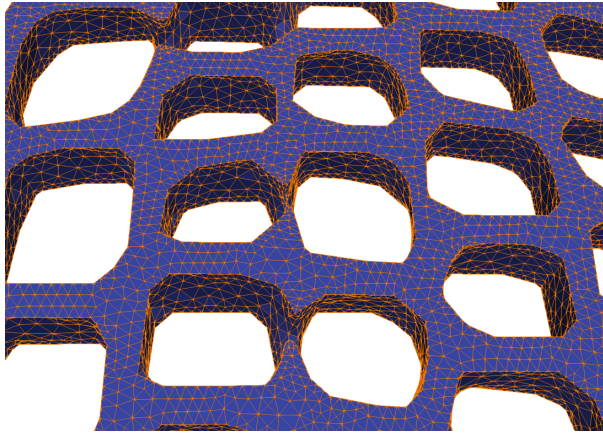


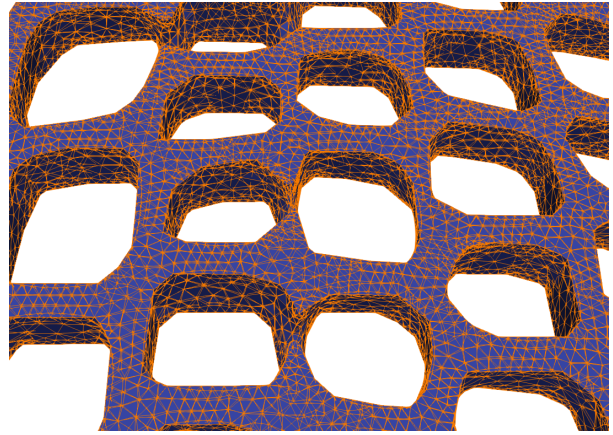
Figure 7: Flow chart to ensure the convergence and set-up scheduling the REV size.

Specimen	Mesh type	Cell number	Voxels	Volume fraction	E_T^{Eff} (MPa)	E_R^{Eff} (MPa)
Spruce	Coarse	228.791	$192 \times 192 \times 6$	0.367	987	1050
	Medium	311.938	$192 \times 192 \times 6$	0.367	900	987
	Refine	540.729	$192 \times 192 \times 6$	0.361	862	932
Poplar	Coarse	482.399	$380 \times 345 \times 9$	0.307	139	255
	Medium	756.203	$380 \times 345 \times 9$	0.307	106	199
	Refine	1.622.184	$380 \times 345 \times 9$	0.303	96	222

Table 1: The effect of meshing process on the spruce and poplar samples.



(a) Coarse mesh.



(b) Refined mesh.

Figure 8: An enlargement of coarse and refined mesh zones for the intermediate spruce specimen with dimension $192 \times 192 \times 6$.

N° REV	Size in voxel	Cell number	Volume fraction	E_R^{Eff} (MPa)	E_T^{Eff} (MPa)
1	$192 \times 192 \times 10$	75.263	0.563	2082	1556
2	$192 \times 192 \times 20$	81.339	0.563	2189	1706
3	$192 \times 192 \times 30$	101.753	0.475	1736	1362
4	$192 \times 192 \times 40$	109.242	0.477	1775	1398
5	$192 \times 192 \times 50$	115.370	0.479	1804	1427
6	$192 \times 192 \times 60$	120.401	0.483	1844	1466
7	$192 \times 192 \times 70$	134.473	0.478	1810	1432
8	$192 \times 192 \times 80$	151.955	0.479	1814	1431
9	$192 \times 192 \times 90$	183.737	0.479	1820	1437
10	$192 \times 192 \times 100$	223.411	0.479	1820	1433
11	$192 \times 192 \times 110$	274.278	0.476	1806	1414
12	$192 \times 192 \times 120$	335.900	0.472	1784	1390
13	$192 \times 192 \times 130$	377.461	0.472	1775	1378
14	$192 \times 192 \times 140$	445.745	0.472	1782	1377
15	$192 \times 192 \times 150$	604.740	0.470	1763	1350
16	$192 \times 192 \times 160$	532.384	0.474	1796	1381.
17	$192 \times 192 \times 170$	557.400	0.489	1831	1453
18	$192 \times 192 \times 180$	598.147	0.487	1795	1409
19	$192 \times 192 \times 190$	650.010	0.489	1836	1452
20	$192 \times 192 \times 200$	699.557	0.486	1790	1399

Table 2: The explanation of the longitudinal effective mechanical properties of the spruce sample in terms of the REV size and informations from the mesh.

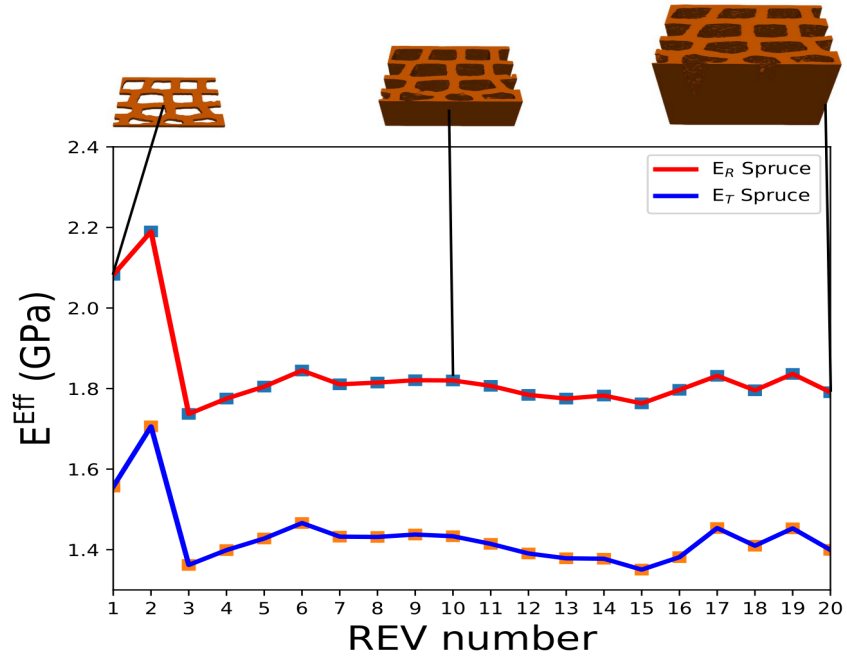


Figure 9: Convergence of the macroscopic Young's modulus in the case of the spruce wood. This convergence is aimed in the longitudinal direction (L) in term of REV defined by (16).

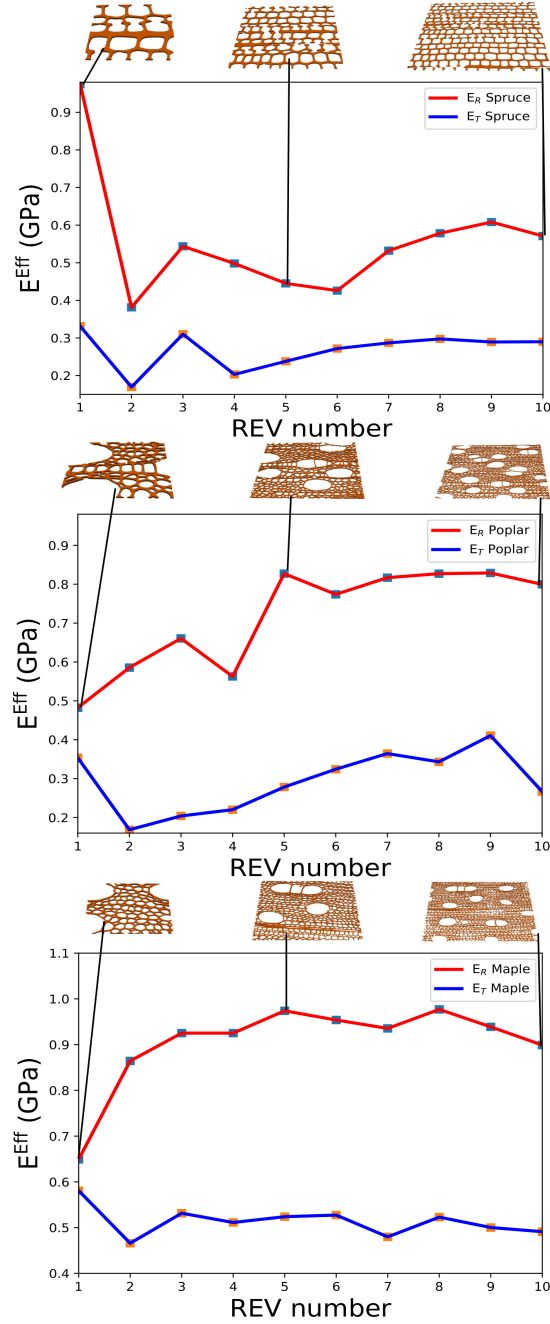
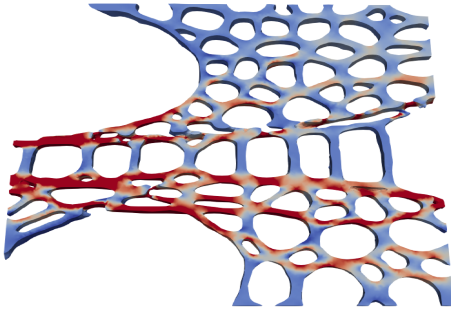


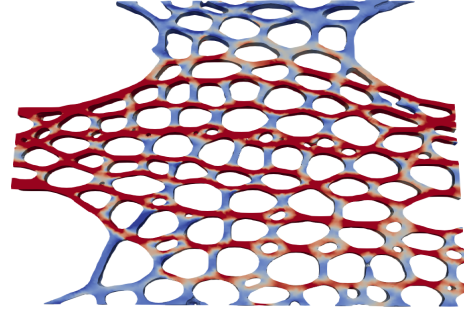
Figure 10: Convergence of the macroscopic Young's modulus in the case of the spruce, poplar, and maple species. This convergence is conducted in the transverse plane (R,T) in term of REV defined in relation (17).

Specimen	N ^o REV	Size in voxel	Cell number	Volume fraction	E_T^{Eff} (MPa)	E_R^{Eff} (MPa)
Spruce	1	192 × 192 × 6	70.811	0.255	331	975
	2	256 × 256 × 6	130.103	0.278	169	381
	3	320 × 320 × 6	198.435	0.298	310	543
	4	384 × 384 × 6	286.267	0.311	203	498
	5	448 × 448 × 6	376.485	0.332	238	445
	6	512 × 490 × 6	497.632	0.320	271	425
	7	576 × 576 × 6	606.485	0.329	286	532
	8	640 × 640 × 6	732.556	0.325	297	578
	9	704 × 704 × 6	870.257	0.320	289	608
	10	768 × 768 × 6	1.039.558	0.318	290	571
Poplar	1	192 × 192 × 6	133.723	0.284	353	482
	2	256 × 256 × 6	247.039	0.301	168	585
	3	320 × 320 × 6	401.630	0.314	204	660
	4	384 × 384 × 6	597.862	0.298	220	562
	5	448 × 448 × 6	838.734	0.344	278	827
	6	512 × 512 × 6	1.049.153	0.335	324	773
	7	576 × 576 × 6	1.278.623	0.319	364	816
	8	640 × 640 × 6	1.590.835	0.322	343	827
	9	704 × 704 × 6	3.176.169	0.346	410	828
	10	768 × 768 × 6	3.653.953	0.345	266	799
Maple	1	192 × 192 × 6	1.609.65	0.313	487	916
	2	256 × 256 × 6	246.450	0.310	583	658
	3	320 × 320 × 6	418.806	0.307	465	864
	4	384 × 384 × 6	556.532	0.337	443	620
	5	448 × 448 × 6	919.130	0.339	523	953
	6	512 × 512 × 6	1.143.100	0.340	527	972
	7	576 × 576 × 6	1.470.580	0.334	479	935
	8	640 × 640 × 6	1.849.768	0.340	522	976
	9	704 × 704 × 6	2.178.739	0.346	500	938
	10	768 × 768 × 6	2.587.940	0.345	492	905

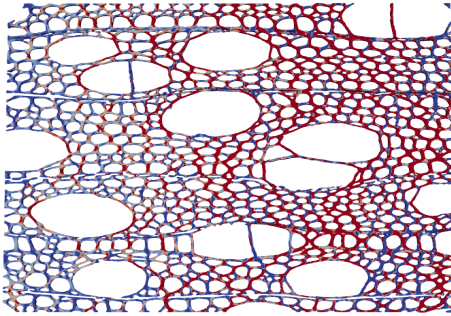
Table 3: The macroscopic Young’s modulus and solid fraction of spruce, poplar, and maple in the orthotropic directions as a function of the REV size.



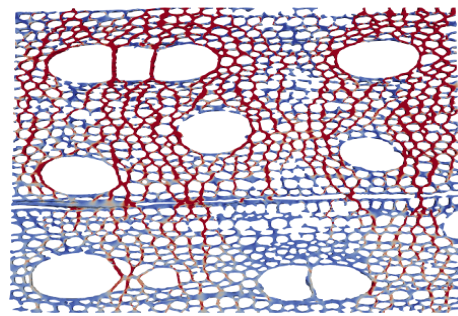
(a) Radial transfert for poplar specimen with dimension $REV_1 = 192 \times 192 \times 6$.



(b) Radial transfert for maple specimen with dimension $REV_1 = 192 \times 192 \times 6$.

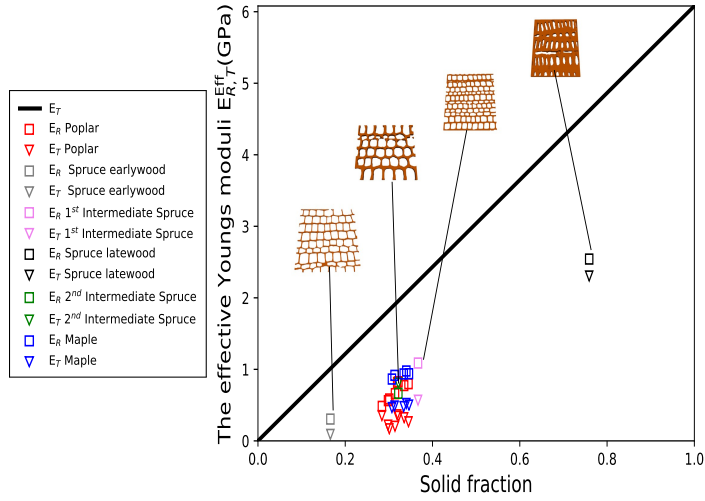


(c) Tangential transfert for poplar specimen with dimension $REV_8 = 640 \times 640 \times 6$.

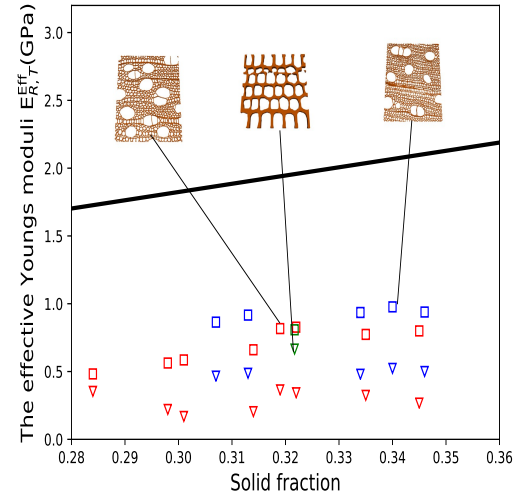


(d) Tangential transfert for maple specimen with dimension $REV_8 = 640 \times 640 \times 6$.

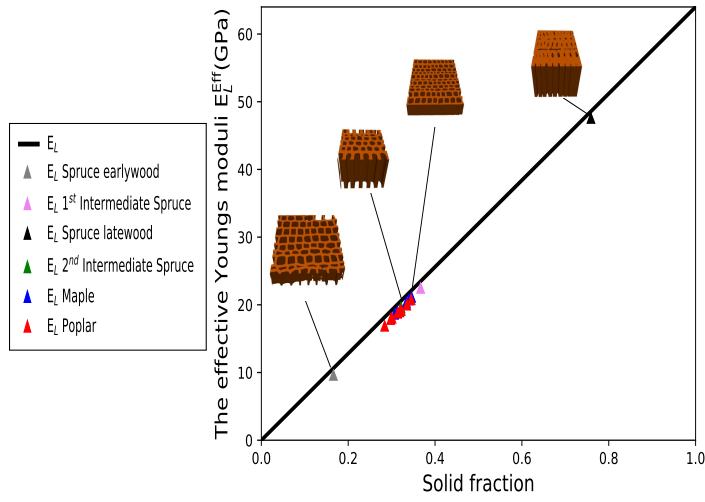
Figure 11: Snapshots of radial and tangential transferts of some wood species under tension.



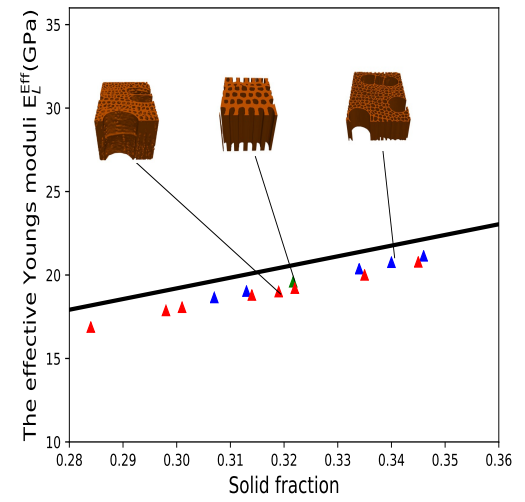
(a) Young's moduli E_R^h/E_T^h .



(b) Young's moduli E_R^h/E_T^h over zone.

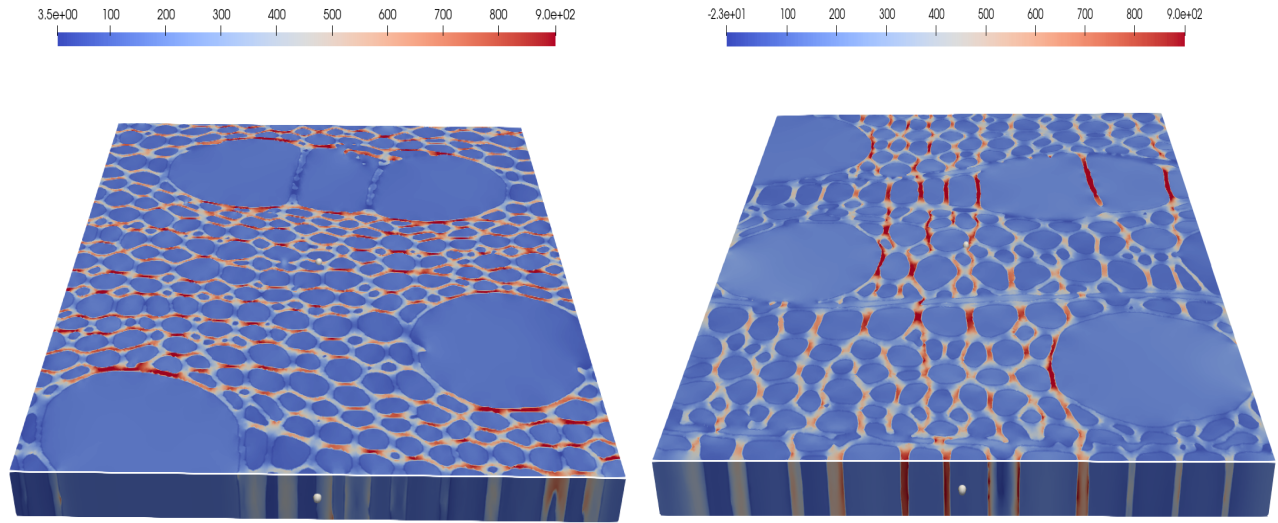


(c) Young's moduli E_L^h .



(d) Young's moduli E_L^h over zone.

Figure 12: The passage from the microscopic scale to the macroscopic one is realized thanks to the homogenization approach. The effective material properties of wood species in their orthotropic directions are presented in each diagram. The solid line refers to the parallel model.



(a) Radial stress σ_{11} under tension $\vec{e}_x(\mathbf{R})$.

(b) Tangential stress σ_{22} under tension $\vec{e}_y(\mathbf{T})$.

Figure 13: (a)-(b) design respectively the radial and tangential tensile stresses for maple and poplar specimens via heterogeneous FE modeling.

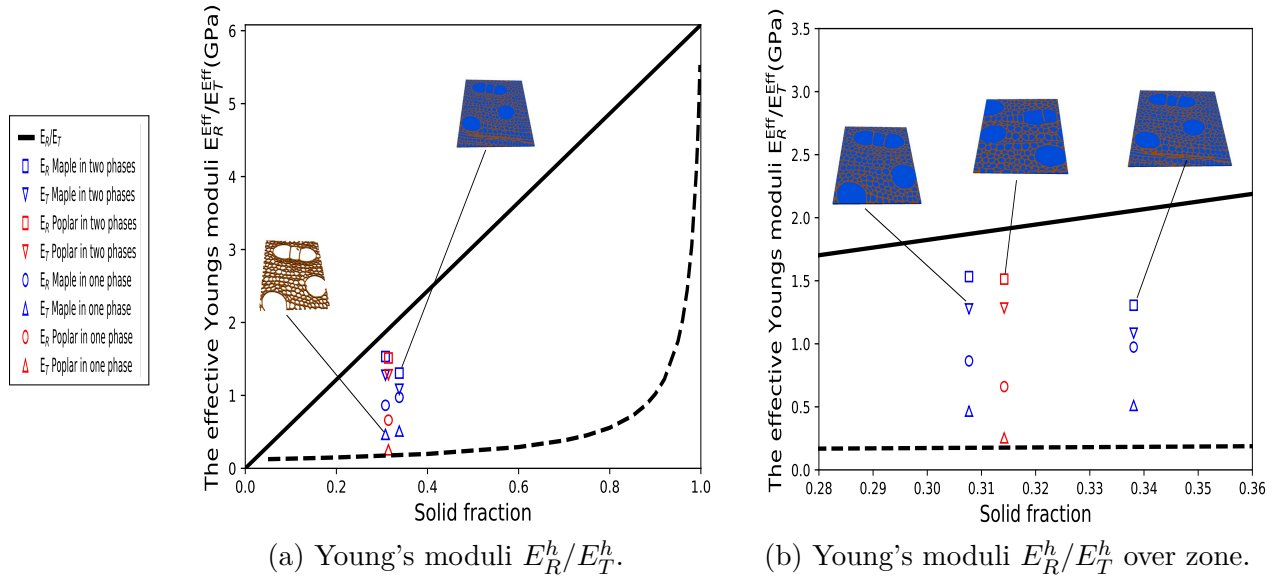


Figure 14: Upscaling strategy, such as the homogenization approach, is used to obtain the effective material properties of wood species over all phases compared with the homogeneous model at the macroscale.